Charge transport modelling of perovskite solar cells accounting for non-Boltzmann statistics in organic and highly-doped transport layers

Will Clarke,[1] Matthew Wolf,[2,3] Alison Walker,[3] and Giles Richardson[1]

[1] *Mathematical Sciences, University of Southampton, UK*
[2] *Institute of Physical Chemistry, RWTH Aachen, Germany*
[3] *Department of Physics, University of Bath, UK*

(Dated: March 16, 2023)

We present a drift-diffusion model of a perovskite solar cell (PSC) in which carrier transport in the charge transport layers is not based on the Boltzmann approximation to the Fermi-Dirac statistical distribution, in contrast to previously studied models. At sufficiently high carrier densities the Boltzmann approximation breaks down and the precise form of the density of states function (often assumed to be parabolic) has a significant influence on carrier transport. In particular, parabolic, Kane and Gaussian models of the density of states are discussed in depth and it is shown that the discrepancies between the Boltzmann approximation and the full Fermi-Dirac statistical model are particularly marked for the Gaussian model, which is typically used to describe organic semiconducting transport layers. Comparison is made between full device models, using parameter values taken from the literature, in which carrier motion in the transport layers is described using (I) the full Fermi-Dirac statistical model and (II) the Boltzmann approximation. For a representative TiO_2/MAPI/Spiro device the behaviour of the PSC predicted by the Boltzmann-based model shows significant differences compared to that predicted by the Fermi-Dirac-based model. This holds both at steady-state, where the Boltzmann treatment overestimates the power conversion efficiency by a factor of 27%, compared to the Fermi-Dirac treatment, and in dynamic simulations of current-voltage hysteresis and electrochemical impedance spectroscopy. This suggests that the standard approach, in which carrier transport in the transport layers is modelled based on the Boltzmann approximation, is inadequate. Furthermore, we show that the full Fermi-Dirac treatment gives a more accurate representation of the steady-state performance, compared to the standard Boltzmann treatment, as measured against experimental data reported in the literature for typical TiO_2/MAPI/Spiro devices.

Keywords: Perovskite solar cells · Drift-diffusion · transport layers · statistical models · organic semiconductors

I. INTRODUCTION

Over the past decade, perovskite solar cells (PSCs) have seen rapid developments, in both efficiency and stability, to an extent that they are now viewed as a realistic prospective next-generation photovoltaic technology. However despite the impressive efficiency of modern PSCs (the current record for certified power conversion efficiency (PCE) is 25.7% [1]), challenges remain that must be overcome to enable large-scale commercial manufacture of perovskite solar panels, the chief amongst these being their relatively poor long-term stability and the presence of lead in the perovskite structure. An increased understanding of the fundamental materials and device physics governing their properties and performance will be key to the further development of PSC technology. In this context, modelling plays a central role in elucidating the basic physical processes underlying the performance of PSCs. In particular, drift-diffusion modelling, which provides a macroscopic description of an entire cell, and directly links to the properties of the materials from which it is constructed, has proven to be a powerful tool to understand PSC device physics [2–4]. PSCs typically use a planar architecture in which a perovskite absorber layer is sandwiched between a highly n-doped electron transport layer (ETL) and a highly p-doped hole transport layer (HTL). While some drift-diffusion models comprising **only** electrons and holes continue to be published [5–7], it has repeatedly been shown that migration of ion vacancies is not only present in the perovskite layer but vital to understanding their operation [8–10]. These simplistic models, which omit ion migration, are incapable of replicating the dynamic current-voltage or impedance responses of PSCs [2, 8, 11–14]. The transport layers are chosen such that light can enter through one of them, either the ETL (standard architecture) [15] or the HTL (inverted architecture) [16]. While early drift-diffusion models of PSCs omitted the transport layers, focusing on the interplay between electronic and ionic conduction in the perovskite layer [8, 17–19], state of the art models include an explicit description of all three layers [12, 20–22], enabling a number of studies of the important role played by the transport layers, and their interplay with the perovskite layer. Such studies have included investigations of the role of intrinsic materials properties, such as band alignment, carrier mobility [23] and dielectric constants [20], as well as extrinsic properties such as layer thickness [24] and doping densities [20], in determining both steady state [23, 24] and transient [20] cell characteristics.

As with any mathematical model, there are a number of assumptions and approximations that are made in the derivation of the drift–diffusion equations (see, e.g. Ref. [25]). In particular, and as will be discussed in detail in

§II, it is typically assumed that the diffusion coefficient (D) is related to the mobility (μ) via the classical Einstein relation (CER):

$$qD = \mu k_B T;$$

this assumption is equivalent to the assumption that the carrier density is **sufficiently low** that the Fermi–Dirac statistical distribution is well approximated by a Boltzmann distribution (see Section II). When this is not the case, the generalised Einstein relation (GER) must be used instead [26, 27]:

$$qD_n = \mu_n n \frac{\partial E_{f_n}}{\partial n}, \qquad qD_p = -\mu_p p \frac{\partial E_{f_p}}{\partial p},$$

in which E_{f_n} and E_{f_p} are the electron and hole quasi-Fermi levels, respectively. This leads to more complex versions of the drift–diffusion equations, the functional forms of which depend on the density of states of the material, and which are, in general, no longer analytic. Physically, this results in an enhancement of the diffusion coefficient relative to the value from the CER, that increases with the local carrier density [27, 28]. Additionally, it is often assumed implicitly that the mobilities (μ_n and μ_p) do not depend on the carrier density. Some studies [29, 30] contradict this but the functional form of the dependence of mobility on carrier density is still debated [31]. Henceforth, for simplicity, we treat the mobilities as constants.

Tessler and Vaynzof have investigated the validity of the Boltzmann approximation in describing electronic carriers in the perovskite layer of a PSC, assuming a density of states function derived from a parabolic dispersion model, and concluded that, while the approximation is warranted in many scenarios, it can lead to appreciable errors in others [2]. However, conditions under which it is valid are likely to be more limited for the transport layers than the perovskite layer for at least the following three reasons: (i) while the perovskite layer is undoped, the transport layers tend to be heavily doped in order to increase their equilibrium carrier density (and hence also conductivity); (ii) even if the equilibrium carrier density in the bulk of the transport layer is sufficiently low for the Boltzmann approximation to be valid, much higher carrier densities can arise in the regions close to the interfaces between layers [20], or when the device is out of equilibrium; and (iii) as will be discussed in Section III, the range of carrier densities for which the Boltzmann approximation is valid depends strongly on the density of states (DoS) function of the material in question. The physical processes occurring at the material interfaces between the perovskite and the transport layers have been shown to be highly important in explaining the dynamic behaviour of the cell, such as current-voltage hysteresis [32–35] and electrochemical impedance spectroscopy [32]. Point (ii) therefore leads us to conjecture that models based on the Boltzmann approximation in the transport layers are not always appropriate when investigating the dynamic behaviour of PSCs. With reference to point (iii), disordered organic semiconductors, which are often used as one of the transport layers in PSCs, are best described by a Gaussian DoS [36, 37], which is only accurately approximated by the Boltzmann distribution in a far smaller domain than inorganic materials with band structures described by a parabolic DoS [38]. The potential inaccuracies arising from the assumption of the CER have also been recognised by Abdel *et al.* [39, 40] but only addressed for ion vacancies in the perovskite layer, rather than the carriers in the transport layers.

In light of the above discussion, the purpose of this contribution is to investigate the effects of full Fermi-Dirac (FD) statistics in drift–diffusion models of PSC devices, with a particular focus on the transport layers. We note that the three-layer drift-diffusion model is sufficiently complex that it is difficult to predict, without the aid of a full numerical solution of the model, exactly how errors associated with employing the Boltzmann approximation in one of the TLs might manifest themselves in the predicted device behaviour in any particular scenario. For example, the accumulation of carriers near the perovskite interface is dependent on the distribution of ion vacancies in the perovskite, which itself is dependent on many material parameters as well as external conditions, such as temperature, light intensity, and applied voltage [20]. Here we shall present example numerical results for a typical three layer device. In particular, we compare the prediction made using a model in which carrier transport in the transport layers is described using full Fermi-Dirac statistics to one in which carrier transport in the transport layers is described using the Boltzmann approximation. Since we consider only a single typical device there remains room for further investigation for other device configurations.

The remainder of the paper is organised as follows. We begin, in §II by discussing the drift-diffusion equations in which carrier transport is modelled using (i) the Boltzmann approximation and (ii) full FD statistics. We further show that the application of full FD statistics causes a density-dependent diffusivity enhancement (equivalent to the generalised Einstein relation), the form of which is determined by the DoS function. Then, in §III, we consider the form of the density of states function for both ordered inorganic and disordered organic materials, and show that the choice of DoS function must be carefully considered in scenarios for which the Boltzmann approximation does not hold. The range of carrier densities for which Boltzmann statistics accurately approximate full FD statistics is discussed for a variety of relevant transport layer materials in §IV. In §V, comparisons are made between the predictions of a device-level model of a PSC in which charge carrier motion in the transport layers is modelled by (i) the Boltzmann approximation and (ii) full FD statistics. The results obtained using these two different descriptions of the transport layers are compared for both steady state performance and transient measurements, namely current-voltage hysteresis and impedance spectroscopy. Finally, we draw our conclusions in §VI.

II. THE DRIFT–DIFFUSION EQUATIONS AND THE GENERALISED EINSTEIN RELATION

The basis of the drift–diffusion model is a set of conservation equations, one for each particle species, in which the change in the particle number density is driven by the net flux into a region and contributions from volume source and sink terms. In most photovoltaic devices the only particle species modelled by the drift-diffusion equations are the charge carriers, *i.e.* electrons in the conduction band (volume density n) and holes in the valence band (volume density p). The source and sink terms in the corresponding conservation equations model photogeneration and recombination, respectively. In halide perovskites it is also necessary to model the transport of one or more mobile point defect species, such as charged anion or cation vacancies [8]. However, it is usually assumed that any defects/dopants in the charge transport layers, which are our focus here, are static and homogeneously distributed.

In one dimension, the case to which we restrict ourselves here, the electron and hole conservation equations take the form

$$\frac{\partial n}{\partial t} = \frac{1}{q}\frac{\partial j^n}{\partial x} + G(x,t) - R(n,p), \tag{1a}$$

$$\frac{\partial p}{\partial t} = -\frac{1}{q}\frac{\partial j^p}{\partial x} + G(x,t) - R(n,p), \tag{1b}$$

in which $G(x,t)$ and $R(n,p)$ are the rates of generation and recombination of electron-hole pairs per unit volume, respectively, and j^n and j^p are the electron and hole current densities, respectively. The latter are calculated from the carrier densities and the quasi-Fermi levels via the relations

$$j^n = \mu_n n \frac{\partial E_{f_n}}{\partial x}, \tag{2a}$$

$$j^p = \mu_p p \frac{\partial E_{f_p}}{\partial x}, \tag{2b}$$

where μ_n and μ_p are the electron and hole mobilities, while E_{f_n} and E_{f_p} are the quasi-Fermi levels of the electrons in the conduction band and holes in the valence band, respectively. The implicit assumption made in using quasi-Fermi levels to characterise the state of the semiconductor is that the valence band electrons are (locally) in thermal equilibrium with each other and that the conduction band electrons are (locally) in thermal equilibrium with each other, but that valence and conduction band electrons are not necessarily in thermal equilibrium with each other. Constitutive equations that relate the quasi-Fermi levels to n, p and ϕ, and which derive from the statistical distributions of the electrons in the valence and conduction bands, must also be specified. The system of drift-diffusion equations is closed by Poisson's equation for the electric potential ϕ,

$$\frac{\partial^2 \phi}{\partial x^2} = -\frac{\rho}{\varepsilon}, \tag{3}$$

where $\rho = q(p-n)$ is the net charge density and ε is the permittivity of the material.

The quasi-Fermi levels depend on the carrier density and the electric potential as follows:

$$E_{f_n} = F_n(n,T) - q\phi, \tag{4a}$$

$$E_{f_p} = F_p(p,T) - q\phi, \tag{4b}$$

where $F_{n,p}$ are functions that depend on both the band structure and the statistical distribution, the forms of which shall be derived below. The current densities (2) can thus be split into a diffusion term and a drift term, as follows:

$$j^n = \mu_n n \frac{\partial E_{f_n}}{\partial n}\frac{\partial n}{\partial x} - q\mu_n n \frac{\partial \phi}{\partial x}, \tag{5a}$$

$$j^p = \mu_p p \frac{\partial E_{f_p}}{\partial p}\frac{\partial p}{\partial x} - q\mu_p p \frac{\partial \phi}{\partial x}. \tag{5b}$$

We define the chemical diffusivities of electrons and holes, respectively, according to Fick's law,

$$qD_n = \mu_n n \frac{\partial E_{f_n}}{\partial n}, \tag{6a}$$

$$qD_p = -\mu_p p \frac{\partial E_{f_p}}{\partial p}, \tag{6b}$$

where the change in sign between the electron and hole diffusivities is due to the sign of their respective charges. This result, referred to as the generalised Einstein relation (GER) [26, 27], allows the current equations to be written as

$$j^n = qD_n \frac{\partial n}{\partial x} - q\mu_n n \frac{\partial \phi}{\partial x}, \tag{7a}$$

$$j^p = -qD_p \frac{\partial p}{\partial x} - q\mu_p p \frac{\partial \phi}{\partial x}. \tag{7b}$$

When the conduction electrons and valence holes satisfy Boltzmann statistics (as is frequently assumed in semiconductor modelling [2, 41–45]), the dependencies of the QFLs on carrier density (*i.e.* the $F_{n,p}$ functions in equations (4)) are logarithmic (a result that will be derived in the following sections). In such scenarios it is straightforward to show that the GER is replaced by the classical Einstein relation,

$$qD_{n,p} = \mu_{n,p} k_B T, \tag{8}$$

in which the ratio of diffusivity to mobility is constant, *i.e.* not dependent on the local carrier concentration. While this approximation greatly simplifies the model, the accuracy of the CER is often poor (as will be shown). In such scenarios the full GER is required.

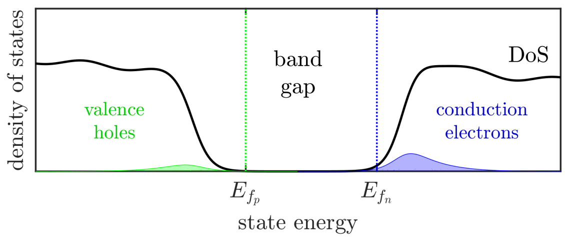

FIG. 1. The filling of electron states. The solid black line shows the density of states (DoS) function $\hat{g}(E)$, solid coloured lines show the density of filled states per unit energy (specifically, $\hat{g}(E)f(E;E_{f_n})$ for conduction electrons and $\hat{g}(E)[1-f(E;E_{f_p})]$ for valence holes), and shaded areas show the total carrier density, integrated over all energies. Here the electron QFL is closer to the band edge than the hole QFL, meaning a higher density of electrons than holes.

A. Statistical integrals and the Fermi level

In order to determine equations for the electron and hole current currents from (2), expressions for the quasi-Fermi levels in terms of the carrier densities are required. In thermal equilibrium, the probability (f) that an electronic state with energy E is occupied in a material with Fermi level E_f is given by the Fermi–Dirac statistical distribution,

$$f(E;E_f) = \frac{1}{\exp\left(\frac{E-E_f}{k_BT}\right)+1}. \tag{9}$$

where T is temperature and k_B is Boltzmann's constant. The density (per unit volume) of electrons lying in the conduction band with energies between E and $E+dE$ is therefore given by the product of the Fermi–Dirac distribution, f, and the density of states (per unit volume), or DoS, $\hat{g}(E)dE$. The corresponding density of holes in the valence band is given by the product of $(1-f)$ with the DoS in the valence band $\hat{g}(E)dE$.

Under the assumption that the material is a semiconductor, we first split the density of states (DoS) $\hat{g}(E)$ into that pertaining to the valence band $\hat{g}_v(E)$ and that pertaining to the conduction band $\hat{g}_c(E)$ (see Figure 1) and write

$$\hat{g}(E) = \hat{g}_v(E) + \hat{g}_c(E). \tag{10}$$

It is usually assumed that the bands are perfectly distinct, meaning there exists a finite range of energies between the highest occupied state and the lowest unoccupied state at absolute zero in which the DoS is zero. However, in the case of organic semiconductors the bands do not have well-defined edges (see Figure 2) and this can lead to definitions of $\hat{g}_v(E)$ and $\hat{g}_c(E)$ which are convenient, but for which there is some overlap of the tails of both functions. We assume that the bands have sufficient separation that any overlap in the DoS functions is negligible and note that any material that violates this would be a poor semiconductor. The total electron and hole densities (per unit volume) are thus

$$n = \int_{-\infty}^{\infty} f(E;E_{f_n})\hat{g}_c(E)dE, \tag{11a}$$

$$p = \int_{-\infty}^{\infty} \left[1 - f(E;E_{f_p})\right]\hat{g}_v(E)dE, \tag{11b}$$

where the Fermi level E_f in the Fermi–Dirac statistical distribution (9) is replaced by the QFL in the conduction/valence band in the expression for the electron/hole density.

For convenience, it is also assumed that the conduction and valence band DoS functions can each be cast in terms of (at least) two dimensional constants, an effective DoS (g_c or g_v) and reference energies E_c or E_v, corresponding to the conduction and valence band edges (in the case of inorganic semiconductors) and to the LUMO and HOMO (in the case of organic semiconductors). The dimensionless functions $\hat{N}_c$ and $\hat{N}_v$ are used to describe the general shape of the density of states function in the vicinity of the reference energies E_c and E_v, respectively. This allows us to write:

$$\hat{g}_c(E) = \frac{g_c}{k_BT}\hat{N}_c\left(\frac{E-E_c}{k_BT}\right), \tag{12a}$$

$$\hat{g}_v(E) = \frac{g_v}{k_BT}\hat{N}_v\left(-\frac{E-E_v}{k_BT}\right), \tag{12b}$$

where $\hat{N}_c$ and $\hat{N}_v$ are here referred to as reduced densities of states. These reduced DoS functions can be obtained from the DoS functions defined in (10) by inverting (12) to obtain

$$\hat{N}_c(\eta) = \frac{k_BT}{g_c}\hat{g}_c\left(E_c + k_BT\eta\right), \tag{13a}$$

$$\hat{N}_v(\eta) = \frac{k_BT}{g_v}\hat{g}_v\left(E_v - k_BT\eta\right), \tag{13b}$$

in which η can be interpreted as a dimensionless state energy level. With these DoS functions, and substituting the Fermi-Dirac distribution (9), the electron and hole densities (11) become

$$n = g_c\int_{-\infty}^{\infty}\frac{1}{k_BT}\frac{\hat{N}_c\left(\frac{E-E_c}{k_BT}\right)}{1+\exp\left(\frac{E-E_{f_n}}{k_BT}\right)}dE, \tag{14a}$$

$$p = g_v\int_{-\infty}^{\infty}\frac{1}{k_BT}\frac{\hat{N}_v\left(-\frac{E-E_v}{k_BT}\right)}{1+\exp\left(\frac{E_{f_p}-E}{k_BT}\right)}dE. \tag{14b}$$

Carrier densities and quasi-Fermi levels are therefore related by an integral dependent on the reduced DoS. Specifically, the carrier densities are given by the expressions

$$n = g_c\mathcal{S}_c\left(\frac{E_{f_n}-E_c}{k_BT}\right), \tag{15a}$$

$$p = g_v\mathcal{S}_v\left(-\frac{E_{f_p}-E_v}{k_BT}\right), \tag{15b}$$

where the **statistical integrals**, $\mathcal{S}_c$ and $\mathcal{S}_v$, are the functions defined by the relations

$$\mathcal{S}_c(\xi) = \int_{-\infty}^{\infty} \frac{\hat{N}_c(\eta)}{1+\exp(\eta-\xi)} d\eta, \tag{16a}$$

$$\mathcal{S}_v(\xi) = \int_{-\infty}^{\infty} \frac{\hat{N}_v(\eta)}{1+\exp(\eta-\xi)} d\eta, \tag{16b}$$

in which ξ may be interpreted as a dimensionless QFL. We note that, in practice, ξ will almost always be negative, meaning both QFLs lie between the two reference energies, E_c and E_v, in the band gap. We invert these expressions (15) for the carrier densities to obtain expressions for the QFLs in terms of the densities. Substituting for the conduction band and valence band reference energies using $E_c = -E_a - q\phi$ and $E_v = -E_a - E_g - q\phi$, leads to the following expressions for the QFLs:

$$E_{f_n} = k_B T \mathcal{S}_c^{-1}\left(\frac{n}{g_c}\right) - E_a - q\phi, \tag{17}$$

$$E_{f_p} = -k_B T \mathcal{S}_v^{-1}\left(\frac{p}{g_v}\right) - E_a - E_g - q\phi, \tag{18}$$

where $\mathcal{S}^{-1}$ is the inverse of $\mathcal{S}$. Here E_a denotes the electron affinity, the difference between the conduction band reference energy and the vacuum level, and $E_g = E_c - E_v$ is the gap between the two bands' reference energies. Note that energies are defined relative to the vacuum level at $E = 0$ eV. In turn, the diffusion coefficients can be calculated as functions of mobility and carrier density from the generalised Einstein relations (6):

$$qD_n = \mu_n k_B T n \frac{\partial}{\partial n}\left(\mathcal{S}_c^{-1}\left(\frac{n}{g_c}\right)\right), \tag{19a}$$

$$qD_p = \mu_p k_B T p \frac{\partial}{\partial p}\left(\mathcal{S}_v^{-1}\left(\frac{p}{g_v}\right)\right). \tag{19b}$$

Equivalently, the expressions for the QFLs (17)-(18) can be substituted directly into the current density equations (2) to obtain the following expressions for the currents:

$$j^n = \mu_n k_B T \left(\Delta_n(n)\frac{\partial n}{\partial x} - \frac{qn}{k_B T}\frac{\partial \phi}{\partial x}\right), \tag{20a}$$

$$j^p = -\mu_p k_B T \left(\Delta_p(p)\frac{\partial p}{\partial x} + \frac{qp}{k_B T}\frac{\partial \phi}{\partial x}\right), \tag{20b}$$

in which

$$\Delta_n(n) = n\frac{\partial}{\partial n}\left(\mathcal{S}_c^{-1}\left(\frac{n}{g_c}\right)\right), \tag{21a}$$

$$\Delta_p(p) = p\frac{\partial}{\partial p}\left(\mathcal{S}_v^{-1}\left(\frac{p}{g_v}\right)\right). \tag{21b}$$

are carrier density-dependent diffusion enhancement functions that approach 1 in the limit of low carrier density [46–50], as will be shown below.

B. The Boltzmann approximation and the classical Einstein relation

It is well known that the Fermi-Dirac distribution (9) approaches the Boltzmann distribution,

$$f(E; E_f) \sim \exp\left(-\frac{E-E_f}{k_B T}\right), \tag{22}$$

for energies significantly greater than the Fermi level, $(E - E_f)/k_B T \gg 1$. Thus, for Fermi energies sufficiently far away from the reference energy of the DoS, the Fermi-Dirac distribution (9) in the statistical integral can be approximated by a Boltzmann distribution (22), and the statistical integral (16) becomes

$$\mathcal{S}(\xi) \approx \int_{-\infty}^{\infty} \hat{N}(\eta)\exp(\xi-\eta)\, d\eta, \tag{23}$$

which can be evaluated as

$$\mathcal{S}(\xi) \approx A \exp(\xi), \tag{24}$$

where

$$A = \int_{-\infty}^{\infty} \hat{N}(\eta)\exp(-\eta)\, d\eta \tag{25}$$

is a scaling constant determined by the reduced DoS, which can readily be reabsorbed into an effective DoS constant. Specifically, this scaling constant is large if there is a high density of states at energies below the reference energy, *i.e.* the DoS has a tail, decaying into the band gap. This approximation, often referred to as the Boltzmann approximation, is valid when the QFL lies far inside the band gap, *i.e.* $\xi \ll -1$.

Thus, Boltzmann distributed carriers have an exponential statistical integral, regardless of DoS function, with inverse $\mathcal{S}^{-1}(x) = \ln(\frac{x}{A})$. This function can be differentiated exactly, leading to

$$\frac{\partial}{\partial n}\left(\mathcal{S}_c^{-1}\left(\frac{n}{g_c}\right)\right) = \frac{1}{n}, \tag{26a}$$

$$\frac{\partial}{\partial p}\left(\mathcal{S}_v^{-1}\left(\frac{p}{g_v}\right)\right) = \frac{1}{p}, \tag{26b}$$

and the diffusion enhancement functions (21) therefore become $\Delta \equiv 1$, thus recovering the classical Einstein relation from the generalised form.

This result is independent of the value of the constant A. The choice of DoS function is therefore unimportant when the Boltzmann approximation holds. If the approximation does not hold, however, the functional form of the DoS becomes significant and must be carefully considered. Furthermore, the choice of DoS affects the domain of carrier densities for which the Boltzmann approximation does hold, as will be discussed in §IV.

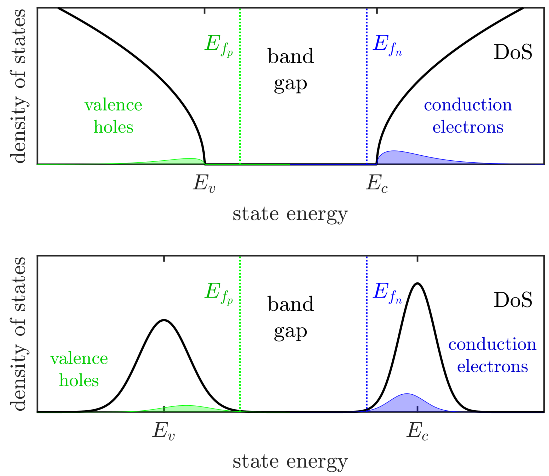

FIG. 2. The filling of electron states in (top) parabolic and (bottom) Gaussian DoS functions.

III. DENSITY OF STATES FUNCTIONS AND STATISTICAL INTEGRALS

A number of different materials have been used as transport layers in PSCs, both inorganic and organic. Charge carrier conduction occurs via different basic mechanisms in the two classes of material (viz. inorganic and organic), which, in the present context, is important because it determines the model for the DoS that is appropriate for a given transport layer material.

Inorganic semiconductors are typically (poly)crystalline with electrons inhabiting delocalised Bloch (travelling) wave states, and the density of states is derived from the (quantum mechanical) dispersion relations of the bands of states. In contrast, electrons in organic materials occupy localised molecular orbitals, and their motion occurs via thermally activated hopping between molecules. In the latter case, a continuous density of states function arises from the (classical) disorder in the molecular arrangements, which causes variations in the energy of the molecular orbitals[1].

As we shall see, in the present context the most important distinction between the two scenarios is that the DoS in a crystalline (inorganic, in this case) material has a well defined minimum, while this is not the case for the amorphous (organic) materials. In this section, we will consider appropriate choices of the DoS function for both crystalline inorganic and amorphous organic materials.

[1] The scenarios described here are, of course, idealisations. Both organic and inorganic materials can exhibit varying degrees of disorder, and intermediate or mixed modes of transport and DoS functions [51–54].

A. Crystalline inorganic materials – Parabolic and simplified Kane Models

As mentioned above, the dispersion relation in an inorganic material has a well defined minimum and maximum. The energy (E) of an electron in a state with wavevector ($\mathbf{k}$) near to the conduction band minimum (with energy E_c and wavevector $\mathbf{k}_c$) can be approximated by an expansion in powers of $|\mathbf{k}-\mathbf{k}_c|$ (see for example [27, 55]). Furthermore, we assume the band structure to be isotropic about this minimum, meaning the expansion depends only on the magnitude $k=|\mathbf{k}-\mathbf{k}_c|$, so that

$$E(k)=E_c+k\frac{\partial E}{\partial k}\bigg|_{k=0}+\frac{k^2}{2}\frac{\partial^2 E}{\partial k^2}\bigg|_{k=0}+\mathcal{O}(k^3). \tag{27}$$

As $k=0$ is the point at which the conduction band has a minimum, the first derivative in this expansion is necessarily zero. Furthermore, on defining the conduction band effective mass by

$$m_c^*=\frac{\hbar^2}{\frac{\partial^2 E}{\partial k^2}\big|_{k=0}}, \tag{28}$$

the following expression for the electron energy is obtained:

$$E-E_c=\frac{\hbar^2}{2m_c^*}k^2. \tag{29a}$$

This is referred to as the parabolic band approximation [55]. Similarly, the dispersion relation in the vicinity of the valence band maximum is

$$E-E_v=-\frac{\hbar^2}{2m_v^*}k^2. \tag{29b}$$

Note that this approximation is based upon a band structure with well-defined valence and conduction band edges that is not found in disordered systems, hence its use is limited to crystalline inorganic materials. The DoS function is then derived according to [27]

$$g(E)=\frac{1}{\pi^2}k^2\frac{dk}{dE} \tag{30}$$

to obtain the DoS functions (as defined in (10)),

$$\hat{g}_c(E)=\frac{2g_c}{\sqrt{\pi}}\left(\frac{1}{k_BT}\right)^{\frac{3}{2}}\sqrt{E-E_c}\quad \text{for } E>E_c, \tag{31a}$$

near the conduction band minimum, and

$$\hat{g}_v(E)=\frac{2g_v}{\sqrt{\pi}}\left(\frac{1}{k_BT}\right)^{\frac{3}{2}}\sqrt{E_v-E}\quad \text{for } E<E_v, \tag{31b}$$

near the valence band maximum. Thus the reduced DoS functions ($\hat{N}_c$ and $\hat{N}_v$, as defined in (13)) have the same form, *i.e.*

$$\hat{N}(\eta)=\begin{cases}0 & \eta<0\\ \frac{2}{\sqrt{\pi}}\sqrt{\eta} & \eta\geq 0.\end{cases} \tag{32}$$

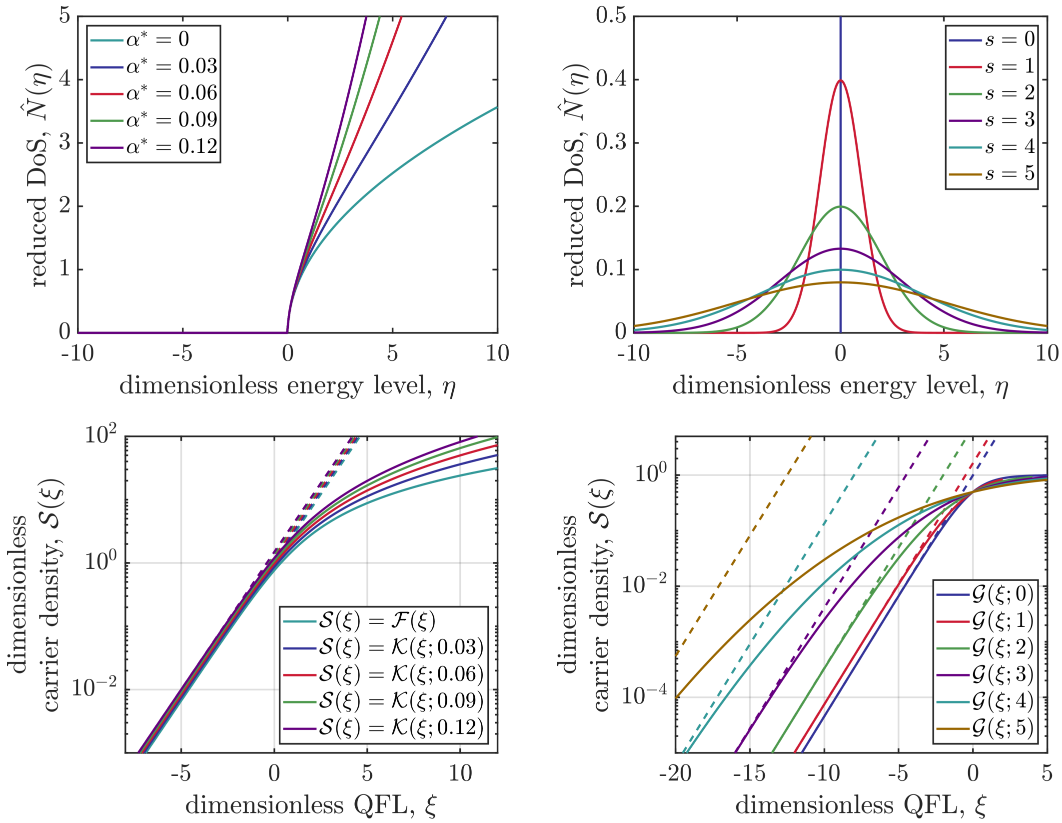

FIG. 3. Reduced densities of state (top) and statistical integrals (bottom) derived from the simplified Kane dispersion (left) and Gaussian disorder (right) models. Solid lines in the bottom plots correspond to full Fermi-Dirac distributions and dashed lines to Boltzmann distributions. Here, $\mathcal{F}, \mathcal{K}$, and $\mathcal{G}$ denote the Fermi–Dirac (33), Kane–Fermi (37), and Gauss–Fermi (41) integrals, α^* is the dimensionless non-parabolicity parameter of the Kane model and s is the dimensionless standard deviation of the Gaussian.

The statistical integral corresponding to this reduced DoS function is $\mathcal{S}_{c,v}(\xi) = \mathcal{F}(\xi)$, where $\mathcal{F}$ follows from (16), and is

$$\mathcal{F}(\xi) = \int_0^\infty \frac{2}{\sqrt{\pi}} \frac{\sqrt{\eta}}{1 + \exp(\eta - \xi)} d\eta, \tag{33}$$

and is referred to as the Fermi-Dirac integral[2].

Further away from the band extrema, the parabolic approximation becomes increasingly inaccurate. States further from the band edge can be modelled by the simplified form of Kane's model for dispersion in III–V semiconductors [57–59], in which (29a) and (29b) are replaced by

$$(E - E_c)\left(1 + \alpha_c(E - E_c)\right) = \frac{\hbar^2}{2m_c^*} k^2 \tag{34a}$$

$$(E - E_v)\left(1 - \alpha_v(E - E_v)\right) = -\frac{\hbar^2}{2m_c^*} k^2 \tag{34b}$$

where α_c and α_v are two parameters that determine the degree of non-parabolicity. We note that the Kane model reduces to the parabolic model in the limit that α goes to zero. Once again, the DoS functions can be derived from (30) to obtain

[2] Specifically, this is the Fermi-Dirac integral of order 1/2 [56]. Note that some definitions omit the prefactor

$$\hat{g}_c(E) = \frac{2g_c}{\sqrt{\pi}}\left(\frac{1}{k_BT}\right)^{\frac{3}{2}}\sqrt{(E-E_c)\left(1+\alpha_c(E-E_c)\right)}\left(1+2\alpha_c(E-E_c)\right), \tag{35a}$$

$$\hat{g}_v(E) = \frac{2g_v}{\sqrt{\pi}}\left(\frac{1}{k_BT}\right)^{\frac{3}{2}}\sqrt{(E_v-E)\left(1+\alpha_c(E_v-E)\right)}\left(1+2\alpha_c(E_v-E)\right). \tag{35b}$$

These Kane DoS functions lead to an altered reduced DoS function taking the place of (32):

$$\hat{N}(\eta) = \begin{cases} 0 & \eta < 0 \\ \frac{2}{\sqrt{\pi}}\sqrt{\eta(1+\alpha^*\eta)}(1+2\alpha^*\eta) & \eta \geq 0, \end{cases} \tag{36}$$

where $\alpha^* = \alpha k_BT$ is the dimensionless non-parabolicity parameter. The statistical integrals for non-parabolic bands are therefore $\mathcal{S}_c(\xi) = \mathcal{K}(\xi;\alpha_c^*)$ for conduction electrons and $\mathcal{S}_v(\xi) = \mathcal{K}(\xi;\alpha_v^*)$ for valence holes, where $\mathcal{K}$ (which follows from (16)) is

$$\mathcal{K}(\xi;\alpha^*) = \int_0^\infty \frac{2}{\sqrt{\pi}}\frac{\sqrt{\eta(1+\alpha^*\eta)}(1+2\alpha^*\eta)}{1+\exp(\eta-\xi)}d\eta, \tag{37}$$

and is referred to here as the Kane-Fermi integral. The non-parabolic DoS function (including the parabolic limit $\alpha \to 0$) and the resulting Kane–Fermi integral are plotted in Figure 3. We note once again that the Kane model reduces to the parabolic model in the limit that $\alpha^* \to 0$, and that therefore the Kane–Fermi integral approaches the Fermi–Dirac integral in the same limit,

$$\lim_{\alpha^*\to 0}\mathcal{K}(\xi;\alpha^*) = \mathcal{F}(\xi). \tag{38}$$

B. Amorphous organic materials – Gaussian model

The discrete transport sites in disordered organic materials are typically modelled by Gaussian DoS functions [36, 38], as represented in Figure 2(b), of the form

$$\hat{g}_c(E) = \frac{g_c}{\sigma_c\sqrt{2\pi}}\exp\left(-\frac{1}{2}\left(\frac{E-E_c}{\sigma_c}\right)^2\right), \tag{39a}$$

$$\hat{g}_v(E) = \frac{g_v}{\sigma_v\sqrt{2\pi}}\exp\left(-\frac{1}{2}\left(\frac{E_v-E}{\sigma_v}\right)^2\right), \tag{39b}$$

where the degree of disorder is represented by the standard deviation, σ. Once again the reduced DoS functions ($\hat{N}_c$ and $\hat{N}_v$) can be obtained using (13) and have the form

$$\hat{N}(\eta, s) = \frac{1}{s\sqrt{2\pi}}\exp\left(-\frac{1}{2}\left(\frac{\eta}{s}\right)^2\right), \tag{40}$$

where $s = \frac{\sigma}{k_BT}$ is the dimensionless disorder parameter, which in general differs between the 'conduction states' (for which the reduced DoS is $\hat{N}(\eta;s_c)$ and and 'valence states' (for which the reduced DoS is $\hat{N}(\eta;s_v)$. The crucial difference from the parabolic model is that the Gaussian band has no defined edge, meaning the reference energies E_c and E_v are now the band centres, the LUMO and HOMO energies, respectively. The statistical integrals (16) resulting from the Gaussian DoS are $\mathcal{S}_c(\xi) = \mathcal{G}(\xi;s_c)$ for conduction electrons and $\mathcal{S}_v(\xi) = \mathcal{G}(\xi;s_v)$ for valence holes, where $\mathcal{G}$ follows from (16):

$$\mathcal{G}(\xi;s) = \frac{1}{s\sqrt{2\pi}}\int_{-\infty}^{\infty}\frac{\exp\left(-\frac{1}{2}\left(\frac{\eta}{s}\right)^2\right)}{1+\exp(\eta-\xi)}d\eta, \tag{41}$$

and is referred to as the Gauss–Fermi integral [60]. The Gaussian DoS function and the resulting Gauss–Fermi integral are plotted in Figure 3. Note that greater standard deviation effectively shifts the onset of the band further away from the reference energy, resulting in a shift in the statistical integral.

IV. ACCURACY OF THE BOLTZMANN APPROXIMATION FOR COMMON TRANSPORT LAYER MATERIALS

As discussed in §II B, the classical Einstein relation (CER) is recovered from the general Einstein relation (GER) when carrier densities are sufficiently low so that the Fermi-Dirac distribution (9) can be approximated by the Boltzmann distribution (22). Under this approximation, the statistical integrals take the form

$$\mathcal{S}(\xi) \approx A\exp(\xi), \tag{24 repeated}$$

where A is some constant determined by the functional form of the reduced DoS (25). For the Kane model (36), this constant is

$$A = \frac{1}{\sqrt{\pi\alpha^*}}e^{\frac{1}{2\alpha^*}}K_2\left(\frac{1}{2\alpha^*}\right) \tag{42}$$

where K_2 is the second order modified Bessel function of the second kind (note that in the limit $\alpha^* \to 0$, the band becomes perfectly parabolic and $A \to 1$). The corresponding result in the Gaussian band model (40) is

$$A = \exp\left(\frac{s^2}{2}\right). \tag{43}$$

Notably, the CER is unaffected by the value of this constant, meaning that **the choice of DoS is unimportant when the Boltzmann approximation holds**.

However, the functional form of the DoS does significantly affect the range of carrier densities in which the Boltzmann approximation holds. Furthermore, as the statistical integrals are not, in general, analytically invertible, the validity of the Boltzmann approximation for each band model usually has to be investigated numerically. In what follows, we conduct such an investigation for a number of different transport layer materials. In particular, we compute the diffusion enhancement factor Δ for some of the more commonly used transport layer materials in PSCs, noting that a value of Δ close to 1 implies that both the CER and the Boltzmann approximation accurately model the material's charge transport properties.

We consider the following inorganic transport layer materials: TiO_2, ZnO and SnO_2 (for the ETL) [61–65], and NiO (for the HTL) [66, 67]. In addition, we consider the following organic transport layer materials: spiro-MeOTAD [68, 69], PEDOT:PSS [70–72] and P3HT [73, 74] (for the HTL), and PCBM [75, 76] (for the ETL). More comprehensive lists of transport layer materials can be found in [77, 78] or through the Perovskite Database Project [79]. The relevant parameters for these transport layer materials, taken from the literature, are shown in Table I. We note that measurements of band nonparabolicity parameters in the literature are rare and, to the authors' knowledge, have not been reported for these materials, possibly because oxides are typically used as insulators in semiconductor applications. In the absence of measured values for inorganic transport layer materials, their bands will be assumed to be perfectly parabolic (i.e. $\alpha^* = 0$).

It is generally agreed that the Boltzmann approximation is sufficiently accurate for carriers in parabolic bands when the QFL is at least three thermal voltages from the band edge ($\xi < -3$), corresponding to carrier concentrations less than $0.05g_{c,v}$. At this carrier density, the diffusion enhancement function, Δ, computed from from full FD statistics (and the GER), is approximately 1.018 and so is within 2% of the value given by the Boltzmann approximation (and the CER). For $\xi > -3$, however, the Boltzmann approximation to the Fermi-Dirac integral begins to overestimate the carrier density, effectively allowing multiple carriers to occupy the same low-energy states. This can be seen in Figure 3, where the Fermi-Dirac integral is plotted with its Boltzmann approximation. The result is that the diffusion enhancement rapidly diverges from 1 as the carrier density exceeds $0.05g_{c,v}$, as shown in Figure 4.

Perhaps unexpectedly, the Boltzmann approximation to the Kane-Fermi integral is accurate over a wider range of densities for greater nonparabolicity. This is because the form of the reduced DoS means nonparabolicity increases the density of higher energy states, far away from the QFL, for the same effective DoS (shown in Figure 3). Despite this, the deviation is minor and the classical Einstein relation can be considered accurate in the same domain as for perfectly parabolic bands.

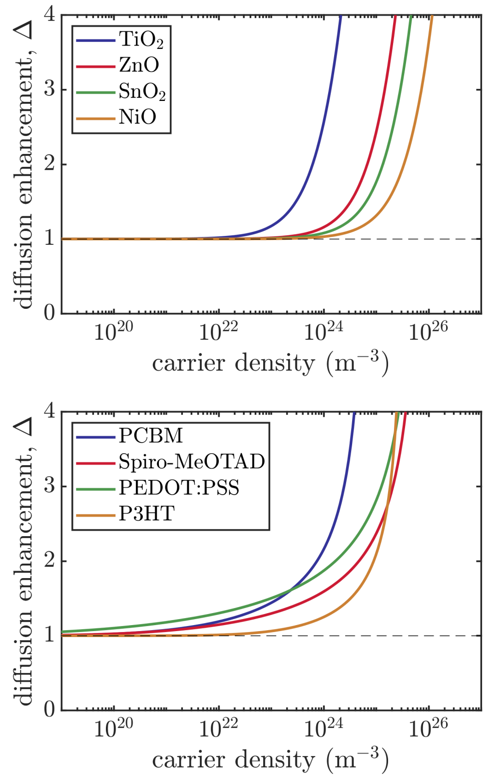

FIG. 4. Diffusion enhancement functions according to the generalised Einstein relation for (top) inorganic and (bottom) organic transport layer materials. Δ is (21a) for ETL materials and (21b) for HTL materials. Similarly, carrier density is n for ETL materials and p for HTL materials. Parameters taken from Table I.

Gaussian bands possess a tail of states extending into the band gap, as shown in Figure 3. These states have energies closer to the QFL, meaning the Boltzmann approximation performs poorly. This is exacerbated by greater disorder [108], as seen in the dependence of the scaling constant for Gaussian bands (43) on the disorder, s. Consequently, the diffusion enhancement function, Δ, predicted by the Gauss-Fermi statistical integral (and the equivalent GER) quickly diverges from 1 (*i.e.* from the value predicted by the Boltzmann approximation and the CER), as shown in Figure 21. The greater the disorder of the material (*i.e.* the larger s is) the more rapid the divergence of Δ away from 1 as the concentration of electrons (or holes) is increased [28].

Measurements of the disorder parameter, s, for common organic PSC transport layer materials taken from the literature are shown in Table I. Values range from 1.04 to 5.38. The corresponding diffusion enhancement functions under the generalised Einstein relation are plotted in Figure 4. Even for the material with the least disorder (P3HT), the GER prediction of Δ has strongly diverged from 1 by the time the carrier density has increased to the typical transport layer doping density. This divergence is far more pronounced for the more

Material	Layer	Record PCE / %	$\mathbf{g_{c,v}}$ / $\mathbf{m^{-3}}$	$\mathbf{E_{c,v}}$ / eV	α^*
Inorganic					
NiO	HTL	20.68 [80]	1.1×10^{25} [81]	-5.41 [82]	N/A
TiO_2	ETL	24.8 [83]	2×10^{23} [81]	-4.13 [84]	N/A
ZnO	ETL	20.09 [85]	2.2×10^{24} [86]	-4.03 [87]	N/A
SnO_2	ETL	25.2 [88]	4.36×10^{24} [89]	-3.91 [90]	N/A
Organic					s
spiro-MeOTAD	HTL	25.2 [88]	1×10^{26} [91]	-5.09 [92]	3.38-4.08 [93–95]
PEDOT:PSS	HTL	21.15 [96]	1×10^{26} [97]	-5.13 [98]	4.09-5.08 [97, 99]
P3HT	HTL	23.9 [100]	4.2×10^{25} [101]	-4.7 [102]	1.04-3.12 [99, 101]
PCBM	ETL	21.43 [103]	$0.1-2\times10^{25}$ [104–106]	-3.95 [107]	2.81-5.38 [104, 105]

TABLE I. Density of states parameters for common PSC transport layer materials. s is the dimensionless width of the Gaussian DoS, $s = \frac{\sigma}{k_B T}$.

disordered materials (such as PEDOT:PSS and PCBM) where it begins at relatively low carrier concentrations.

V. EFFECTS OF FULL FERMI-DIRAC STATISTICS ON DEVICE-LEVEL MODELS

As discussed in the previous section, the diffusion enhancement predicted by charge transport models based upon a full description of the charge carrier statistics (*i.e.* using a full FD statistical model) is often significant in the materials commonly employed as transport layers for PSCs over the range of carrier densities relevant to device operation. In this section, we examine the effect that this more complete physical description of the transport layers has on the predictions of both steady-state and time-dependent device behaviour. In order to do this, we augment the widely-used model of the three-layer planar PSC [2, 12, 13, 19–21, 39, 109], with a model of carrier transport in the transport layers based upon full FD statistics (*i.e.* (20)-(21)), to account for the fact that carrier densities are sufficiently high that the standard Boltzmann approximation breaks down in these layers. We define the statistical integrals as $\mathcal{S}_E$ in the conduction band of the ETL and as $\mathcal{S}_H$ in the valence band of the HTL, and note that the minority carriers in the transport layers (*i.e.* holes in the ETL and electrons in the HTL) typically occur at such low densities that they do not significantly affect device behaviour, and so can be neglected. Since only a single significant carrier species is modelled in each transport layer, we drop the subscripts c and v that distinguish between conduction and valence bands.

The principle change to the standard device model, in which Boltzmann statistics are assumed accurate for all carriers, is that electron and hole current densities in the transport layers are now computed with generalised Einstein relations (GER), via (20)-(21), with an appropriate statistical model and material parameters. The changes to the statistical integrals also lead to minor alterations to the continuity and boundary conditions. These are described in more detail in [110] but the full drift-diffusion model solved here is also stated in Appendix A.

The numerical results presented here are obtained using a recently released version of the open-source PSC simulation software, `IonMonger` [18, 21, 110], which enables the user to simulate a variety of measurement protocols, including current-voltage sweeps and impedance spectroscopy. Details of the numerical methods used for adapting the discretised, non-dimensional charge transport model to account for the GER can be found in [110], along with a discussion of the challenges of implementing statistical integrals, which are neither analytically invertible nor differentiable, without significantly impacting the computation time.

The charge transport model of a PSC discussed here is too complex to easily predict how changes to the statistical models of the transport layers affect the predictions of the cell's response to particular experimental protocols, but appropriate numerical solutions to the model allow us to investigate these changes on a case by case basis. In particular, they offer insight into the scenarios in which the error made by assuming Boltzmann statistics (and correspondingly the CER) leads to significant error in the predicted device behaviour. In order to illustrate our hypotheses we compute solutions based on a representative data set for a TiO_2/MAPI/Spiro-MeOTAD cell (given in Appendix B), with transport layer DoS parameters taken from Table I. We note that, while we construct the parameter set using material parameters taken from independent measurements, simulations using our parameter set may exhibit differences from the behaviour of a real device of this form as a consequence of device construction (*e.g.* material deposition method and architecture). The device considered here is intended to be representative, and a full parameter sweep lies outside the scope of this work.

A. Steady-state performance

Here the effect of the Boltzmann approximation in the transport layers on four key performance parameters is investigated by computing numerical solutions to

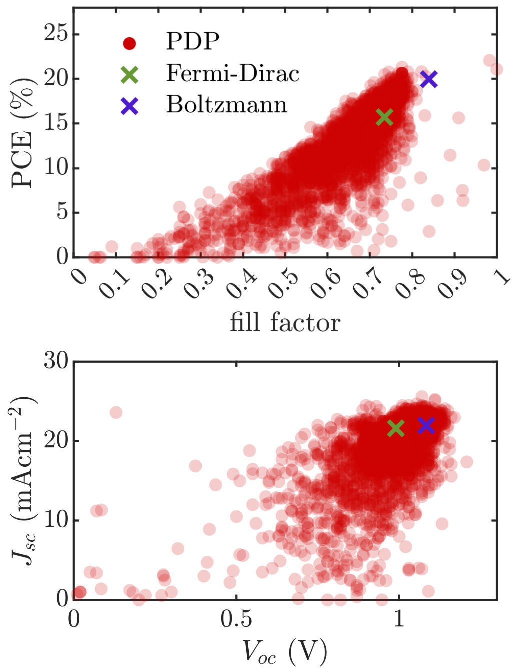

FIG. 5. Measured steady state performance parameters of TiO_2/MAPI/Spiro-MeOTAD cells. Red circles were taken from The Perovskite Database Project [79]. Crosses were obtained through simulations using `IonMonger`, based on the parameter set given in Appendix B. The band shapes in the TiO_2 and in the Spiro-MeOTAD were taken to be parabolic and Gaussian, respectively, using the parameters given in Table I. Significant differences can be observed between the predictions made using the Boltzmann approximation (blue crosses) and full Fermi-Dirac statistics (green crosses).

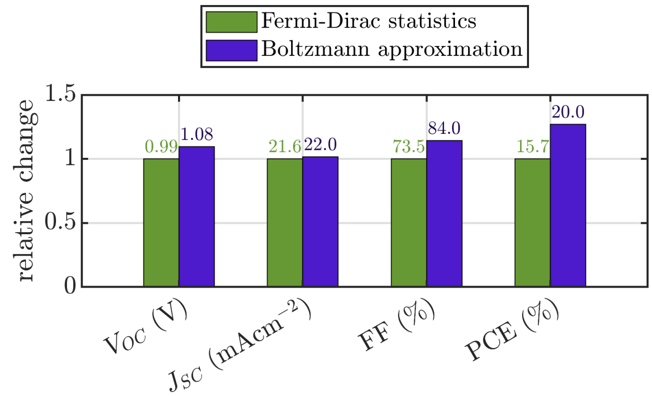

FIG. 6. Sensitivity of key performance parameters to the Boltzmann approximation in the transport layers of a TiO_2/MAPI/Spiro-MeOTAD cell. Obtained through simulation using `IonMonger`. The parameter set is listed in Appendix B. The band shapes in the TiO_2 and Spiro-MeOTAD were parabolic and Gaussian, respectively, with parameters taken from Table I.

the drift-diffusion device model.

Steady-state results are shown in Figures 5 and 6, in which direct comparison is made between the predictions of four key performance parameters (V_{OC}, J_{SC}, fill factor (FF), and power conversion efficiency (PCE)) obtained using full FD statistics in the transport layers (*i.e.* the GER), and those obtained using the Boltzmann approximation (*i.e.* the CER). The short-circuit current (J_{SC}) shows the least sensitivity to the change in the statistical model of the transport layer carriers, a consequence of the low carrier densities in the transport layers at this low voltage. Conversely, the predicted open-circuit voltage (V_{OC}) found using Boltzmann statistics is 9.43% greater than that found using the full statistical models of the TLs. This is a consequence of the Boltzmann approximation being far less accurate at open-circuit, where the large applied voltage leads to large carriers concentrations in the TLs. Combined with an increase in the fill factor (FF), the increase in V_{OC} leads the model based on the Boltzmann approximation to significantly overestimate the PCE of the cell (by a factor of 27.04%). As shown in Figure 5, where simulations are compared to data from the Perovskite Database Project [79], the simulated steady-state performance parameters obtained using simulations based on full FD statistics in the transport layers are more representative of the experimental results found in the literature than those predictions made using simulations based on Boltzmann statistics for this particular device configuration.

The importance of these results lies in the fact that, owing to the difficulty in obtaining accurate estimates of material properties, many parameters are commonly fitted by comparing simulations to experiment, for values such as the short-circuit current and the open-circuit voltage. Thus, if the model predicts these values incorrectly (as seen here), material parameter estimates obtained through fitting will also be incorrect, leading to divergence between fitted parameter values obtained from the same material using different experimental protocols. This is likely to create confusion in the field and lead to difficulty in obtaining reliable and accurate material parameters estimates.

B. Current–voltage hysteresis

Differences in the predictions of PSC behaviour between models based on Boltzmann statistics in the TLs and those based on full FD statistics are not restricted to steady state behaviour. As shown in Figures 7 and 8, simulations of J-V hysteresis and impedance spectroscopy both show significant differences depending on which of these two modelling assumptions is applied.

A 180mVs^{-1} scan of the TiO_2/MAPI/Spiro-MeOTAD parameter set shows that the use of Boltzmann statistics in the transport layers leads not only to a different open-circuit voltage to that predicted by FD statistics, but also to qualitative differences in the shape of the hysteresis curve and the fill factor obtained from each direction of

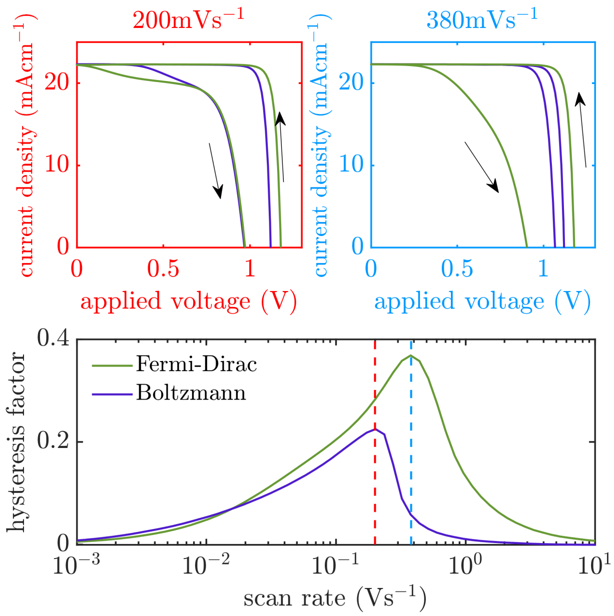

FIG. 7. The effect of the Boltzmann approximation vs. full Fermi-Dirac statistics for current-voltage hysteresis for the parameter set listed in Appendix B. The scan rates showing maximum hysteresis factor under the Boltzmann approximation and Fermi-Dirac statistics are plotted in the top-left and top-right panels respectively.

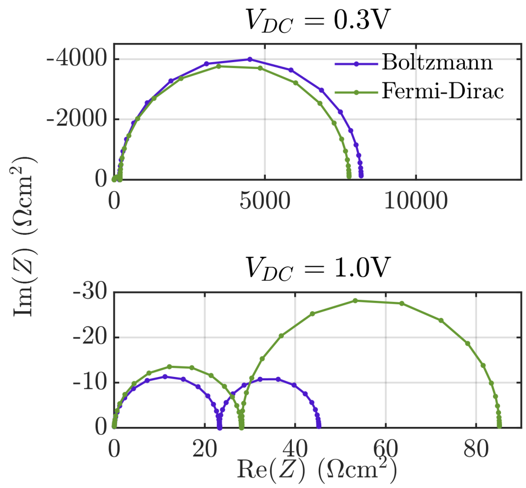

FIG. 8. The effect of the Boltzmann approximation vs. full Fermi-Dirac statistics on impedance spectra for the parameter set listed in Appendix B. The DC voltages were 0.3V (top) and 1.0V (bottom).

the scan. It has long been understood that the observed performance of a PSC during a current-voltage sweep is highly influenced by the preconditioning procedure [8], where the cell is held to equilibrate at a high applied voltage. Changes to the statistical integrals strongly influence the preconditioned state of the cell, and thus have a knock-on effect on the predicted performance observed during the sweep. Once again, the shape of the hysteresis curve is highly sensitive to many material parameters and subtleties of the drift-diffusion model and the effects seen for this parameter set cannot be assumed to be uniform across all other parameter sets.

C. Impedance spectroscopy

Current-voltage sweeps constitute only one of many dynamic characterisation techniques commonly simulated by drift-diffusion models. Another is impedance spectroscopy (IS), in which the steady state is perturbed by a small-amplitude oscillating voltage at varying frequencies and the amplitude and phase of the current response is measured as a function of frequency. This technique can be used to diagnose performance losses and degradation as well as probe the timescales on which the physical processes within the cell operate [13, 111–113]. Recent additions of FD statistics and an IS simulation capability to `IonMonger` [110] provide the first PSC modelling software capable of exploring the interdependent effects of the two. As shown in Figure 8, predicted impedance spectra are highly sensitive to changes in the statistical integrals. The discrepancies between the simulations employing the Boltzmann approximation in the transport layers and those based on FD statistics in the transport layers are exacerbated for larger values of the DC voltage, the value about which the voltage is perturbed, and particularly impact the low-frequency arc, caused by the charging and discharging of the Debye layers and mediated by the mobile ions in the perovskite [13].

VI. CONCLUSION

While the Boltzmann approximation (from which the classical Einstein relation, or CER, is derived) has been widely employed in semiconductor modelling, it has often been used without due consideration of the validity of the approximation in the scenario in which it is being employed. Specifically, the use of organic materials to fabricate PSC transport layers, and the high doping levels in these structures, suggest that the Boltzmann approximation (22) to the Fermi–Dirac statistical distribution (9) (and thus also the CER) is frequently inaccurate in the transport layers. This, in turn, can lead to significant errors in the predictions made by perovskite solar cell charge transport models.

Incorporating a full statistical treatment of the charge carrier dynamics in the transport layers (equivalent to using the generalised Einstein relation) leads to a density-dependent diffusion enhancement function, Δ, that is determined by the density of states (DoS) function. For cases in which the Boltzmann approximation is accurate, the diffusion enhancement function reduces to $\Delta = 1$.

Crucially, however, the function is highly sensitive to the choice of DoS function. In particular, the region of validity of the Boltzmann approximation depends sensitively on the exact DoS employed by the model. Of the common PSC transport layer materials, disordered organic materials, which are usually modelled by a Gaussian DoS function, are those for which the Boltzmann approximation is least accurate, due to the diffuse nature of the Gaussian. The accuracy is particularly poor for the materials with greatest disorder, such as PCBM and PEDOT:PSS.

In order to test the sensitivity of drift-diffusion models of a typical TiO_2/MAPI/Spiro-MeOTAD PSC to changes in the description of carrier transport in the transport layers of the device, comparison was made between predicted device behaviour obtained from (I) a PSC model in which carrier transport in the transport layers was described using the Boltzmann approximation and (II) a PSC model in which full Fermi-Dirac statistics were employed.

Numerical solutions show that the the full statistical treatment of carrier transport in the TLs leads to significantly different predictions of four key steady state performance parameters (V_{OC}, J_{SC}, FF and PCE) in comparison to the predictions made by the model in which carrier transport in the TLs is described by the Boltzmann approximation. The most notable is between the predictions of the PCE, the value of which was overestimated by the model based upon the Boltzmann approximation by 27%. This leads us to conclude that the steady state performance of the cell is not well-described by the standard planar perovskite solar cell model (*i.e.* one in which the Boltzmann approximation is employed in the transport layers). Due to the large number of material parameters in the PSC model and the difficulty in obtaining accurate estimates of their values, it is common to fit some parameters to match experimental data, particularly the four performance parameters considered here. It is clear that fitting these parameters to the standard model (based on the Boltzmann approximation) can easily lead to incorrect predictions of these parameters, and a misleading description of the cell.

In addition to steady state performance, two common dynamic measurements, namely current-voltage hysteresis and impedance spectroscopy, were simulated using PSC models based on (I) a Boltzmann description of the transport layers (TLs) and (II) a full Fermi-Dirac description of the TLs. For this representative parameter set, the model based on the Boltzmann approximation incorrectly predicts both the maximum hysteresis factor and the scan rate at which this maximum appears (Figure 7). Furthermore, the Boltzmann model produces qualitative errors in the shape of the J-V curve across a wide range of physically relevant scan rates. Similar errors were observed in the Boltzmann model when simulating impedance spectroscopy, dependent on the DC voltage. At low voltages, carrier densities in the transport layers near the perovskite interfaces are lower, meaning the Boltzmann approximation is more likely to be accurate. For greater DC voltages, however, carriers in the transport layers accumulate near the perovskite interfaces, affecting the ion vacancy accumulation/depletion occurring on the perovskite side of the interfaces, and thus the low-frequency arc on the Nyquist plot that is caused by ion migration. Recently it has been shown that adopting an asymptotic approach to solving the charge transport model, rather than a numerical one, can provide significant insight into the impedance spectroscopy response of PSCs [112]. Application of these mathematical methods to the modified charge transport model presented here will therefore be the subject of future work, with the aim of elucidating the exact effect of the Boltzmann approximation in IS modelling. The numerical simulations conducted here, however, show that the Boltzmann approximation causes significant errors in predictions of dynamic device-level behaviour.

As understanding of PSC physics continues to improve, it is essential that models of their operation also continue to advance. While PSC drift-diffusion models based on the standard Boltzmann approximation of charge carrier statistics in the transport layers may, in some cases, be sufficient, their validity cannot be assumed in general. In particular, while Boltzmann statistics give a fair description of charge transport in weakly doped and inorganic transport layer materials, they provide a much poorer description of strongly doped and organic transport layer materials. The numerical methods discussed here, and their implementation in `IonMonger`, give the perovskite community access to fast and accurate numerical models incorporating alternative statistical descriptions of charge carrier behaviour in the transport layers that enable simulations of enhanced predictive power, across a wide range of scenarios, which are not solely limited to the steady-state but include current-voltage and impedance spectroscopy measurements.

ACKNOWLEDGEMENTS

WC was supported by an EPSRC grant (reference EP/V520056/1). MW and ABW were supported by the European Commission through the Horizon 2020 Framework Programme for Research and Innovation, Energy Oriented Centre of Excellence (EoCoE-II) project (Grant Agreement ID: 824158).

[1] NREL. Best research-cell efficiency chart, https://www.nrel.gov/pv/cell-efficiency.html (accessed 08/04/2022).

[2] Nir Tessler and Yana Vaynzof. Insights from device modeling of perovskite solar cells. *ACS Energy Letters*, 5(4):1260–1270, 2020.

[3] Vincent M. Le Corre, Zishuai Wang, L. Jan Anton Koster, and Wolfgang Tress. *Device Modeling of Perovskite Solar Cells: Insights and Outlooks*, pages 4–1–4–32. 2020.

[4] Antonio J. Riquelme, Karen Valadez-Villalobos, Pablo P. Boix, Gerko Oskam, Iván Mora-Seró, and Juan A. Anta. Understanding equivalent circuits in perovskite solar cells. insights from drift-diffusion simulation. *Physical Chemistry Chemical Physics*, 24(26):15657–15671, 2022.

[5] Peng Zhao, Jie Su, Zhenhua Lin, Jiaping Wang, Jincheng Zhang, Yue Hao, Xiaoping Ouyang, and Jingjing Chang. The crystal anisotropy effect of mapbi3 perovskite on optoelectronic devices. *Materials Today Energy*, 17:100481, 2020.

[6] Yousaf Hameed Khattak, Faisal Baig, Ahmed Shuja, Lahoucine Atourki, Kashif Riaz, and Bernabé Marí Soucase. Device optimization of pin structured perovskite solar cells: Impact of design variants. *ACS Applied Electronic Materials*, 3(8):3509–3520, 2021.

[7] Ahmed-Ali Kanoun, Souraya Goumri-Said, and Mohammed Benali Kanoun. Device design for high-efficiency monolithic two-terminal, four-terminal mechanically stacked, and four-terminal optically coupled perovskite-silicon tandem solar cells. *International Journal of Energy Research*, 45(7):10538–10545, 2021.

[8] Giles Richardson, Simon E. J. O'Kane, Ralf G. Niemann, Timo A. Peltola, Jamie M. Foster, et al. Can slow-moving ions explain hysteresis in the current–voltage curves of perovskite solar cells? *Energy & Environmental Science*, 9(4):1476–1485, 2016.

[9] Christopher Eames, Jarvist M. Frost, Piers R. F. Barnes, Brian C. O'Regan, Aron Walsh, et al. Ionic transport in hybrid lead iodide perovskite solar cells. *Nature Communications*, 6(1):7497, 2015.

[10] Luca Bertoluzzi, Caleb C Boyd, Nicholas Rolston, Jixian Xu, Rohit Prasanna, Brian C O'Regan, and Michael D McGehee. Mobile ion concentration measurement and open-access band diagram simulation platform for halide perovskite solar cells. *Joule*, 4(1):109–127, 2020.

[11] Mingzhen Liu, Michael B. Johnston, and Henry J. Snaith. Efficient planar heterojunction perovskite solar cells by vapour deposition. *Nature*, 501(7467):395–398, 2013.

[12] Martin T. Neukom, Andreas Schiller, Simon Züfle, Evelyne Knapp, Jorge Ávila, et al. Consistent device simulation model describing perovskite solar cells in steady-state, transient, and frequency domain. *ACS Applied Materials & Interfaces*, 11(26):23320–23328, 2019.

[13] Antonio Riquelme, Laurence J. Bennett, Nicola E. Courtier, Matthew J. Wolf, Lidia Contreras-Bernal, et al. Identification of recombination losses and charge collection efficiency in a perovskite solar cell by comparing impedance response to a drift-diffusion model. *Nanoscale*, 12(33):17385–17398, 2020.

[14] Philip Calado, Andrew M Telford, Daniel Bryant, Xiaoe Li, Jenny Nelson, Brian C O'Regan, and Piers RF Barnes. Evidence for ion migration in hybrid perovskite solar cells with minimal hysteresis. *Nature communications*, 7(1):13831, 2016.

[15] James M. Ball, Michael M. Lee, Andrew Hey, and Henry J. Snaith. Low-temperature processed meso-superstructured to thin-film perovskite solar cells. *Energy & Environmental Science*, 6(6):1739, 2013.

[16] Pablo Docampo, James M. Ball, Mariam Darwich, Giles E. Eperon, and Henry J. Snaith. Efficient organometal trihalide perovskite planar-heterojunction solar cells on flexible polymer substrates. *Nature Communications*, 4(1), 2013.

[17] Stephan Van Reenen, Martijn Kemerink, and Henry J. Snaith. Modeling anomalous hysteresis in perovskite solar cells. *The Journal of Physical Chemistry Letters*, 6(19):3808–3814, 2015.

[18] N. E. Courtier, G. Richardson, and J. M. Foster. A fast and robust numerical scheme for solving models of charge carrier transport and ion vacancy motion in perovskite solar cells. *Applied Mathematical Modelling*, 63:329–348, 2018.

[19] N. E. Courtier, J. M. Foster, S. E. J. O'Kane, A. B. Walker, and G. Richardson. Systematic derivation of a surface polarisation model for planar perovskite solar cells. *European Journal of Applied Mathematics*, 30(3):427–457, 2019.

[20] Nicola E. Courtier, James M. Cave, Jamie M. Foster, Alison B. Walker, and Giles Richardson. How transport layer properties affect perovskite solar cell performance: insights from a coupled charge transport/ion migration model. *Energy & Environmental Science*, 12(1):396–409, 2019.

[21] N. E. Courtier, J. M. Cave, A. B. Walker, G. Richardson, and J. M. Foster. Ionmonger: a free and fast planar perovskite solar cell simulator with coupled ion vacancy and charge carrier dynamics. *Journal of Computational Electronics*, 18(4):1435–1449, 2019.

[22] Philip Calado, Ilario Gelmetti, Benjamin Hilton, Mohammed Azzouzi, Jenny Nelson, and Piers R. F. Barnes. Driftfusion: an open source code for simulating ordered semiconductor devices with mixed ionic-electronic conducting materials in one dimension. *Journal of Computational Electronics*, 2022.

[23] Faiza Azri, Afak Meftah, Nouredine Sengouga, and Amjad Meftah. Electron and hole transport layers optimization by numerical simulation of a perovskite solar cell. *Solar energy*, 181:372–378, 2019.

[24] Abdelkader Hima, Nacereddine Lakhdar, Boubaker Benhaoua, Achour Saadoune, Imad Kemerchou, et al. An optimized perovskite solar cell designs for high conversion efficiency. *Superlattices and Microstructures*, 129:240–246, 2019.

[25] Peter A Markowich, Christian A Ringhofer, and Christian Schmeiser. *Semiconductor equations*. Springer Science & Business Media, 2012.

[26] PT Landsberg. Einstein and statistical thermodynamics. iii. the diffusion-mobility relation in semiconductors. *European Journal of Physics*, 2(4):213, 1981.

[27] Neil W Ashcroft. Solid state physics. *Solid State Physics*, 1:2, 1976.

[28] Yohai Roichman and Nir Tessler. Generalized einstein relation for disordered semiconductors—implications for device performance. *Applied Physics Letters*, 80(11):1948–1950, 2002.

[29] W. F. Pasveer, J. Cottaar, C. Tanase, R. Coehoorn, P. A. Bobbert, P. W. M. Blom, M. D, and M. A. J.

Michels. Unified description of charge-carrier mobilities in disordered semiconducting polymers. *Physical Review Letters*, 94(20), 2005.

[30] Jiu-Xun Sun, Hong-Chun Yang, Yang Li, and Hai-Juan Cui. Unified mobility model for diffusion-limited current in organic diodes based on fermi-dirac statistics. *Physical Review Applied*, 16(3):034037, 2021.

[31] AV Nenashev, JO Oelerich, AV Dvurechenskii, F Gebhard, and SD Baranovskii. Fundamental characteristic length scale for the field dependence of hopping charge transport in disordered organic semiconductors. *Physical Review B*, 96(3):035204, 2017.

[32] Agustin O. Alvarez, Ramón Arcas, Clara A. Aranda, Loengrid Bethencourt, Elena Mas-Marzá, Michael Saliba, and Francisco Fabregat-Santiago. Negative capacitance and inverted hysteresis: Matching features in perovskite solar cells. *The Journal of Physical Chemistry Letters*, 11(19):8417–8423, 2020.

[33] Ilka M. Hermes, Yi Hou, Victor W. Bergmann, Christoph J. Brabec, and Stefan A. L. Weber. The interplay of contact layers: How the electron transport layer influences interfacial recombination and hole extraction in perovskite solar cells. *The Journal of Physical Chemistry Letters*, 9(21):6249–6256, 2018.

[34] Ross A. Kerner and Barry P. Rand. Linking chemistry at the $tio_2ch_3nh_3pbi_3$ interface to current–voltage hysteresis. *The Journal of Physical Chemistry Letters*, 8(10):2298–2303, 2017.

[35] David A. Egger, Achintya Bera, David Cahen, Gary Hodes, Thomas Kirchartz, Leeor Kronik, Robert Lovrincic, Andrew M. Rappe, David R. Reichman, and Omer Yaffe. What remains unexplained about the properties of halide perovskites? *Advanced Materials*, 30(20):1800691, 2018.

[36] S. V. Novikov, D. H. Dunlap, V. M. Kenkre, P. E. Parris, and A. V. Vannikov. Essential role of correlations in governing charge transport in disordered organic materials. *Physical Review Letters*, 81(20):4472–4475, 1998.

[37] Heinz Bässler. Charge transport in disordered organic photoconductors. a monte carlo simulation study. *Physica Status Solidi B (Basic Research);(Germany)*, 175(1), 1993.

[38] Nir Tessler and Yohai Roichman. Amorphous organic molecule/polymer diodes and transistors—comparison between predictions based on gaussian or exponential density of states. *Organic Electronics*, 6(5-6):200–210, 2005.

[39] Dilara Abdel, Petr Vágner, Jürgen Fuhrmann, and Patricio Farrell. Modelling charge transport in perovskite solar cells: Potential-based and limiting ion depletion. *Electrochimica Acta*, 390:138696, 2021.

[40] Dilara Abdel, Nicola Courtier, and Patricio Farrell. Volume exclusion effects in perovskite charge transport modeling. In *2022 International Conference on Numerical Simulation of Optoelectronic Devices (NUSOD)*, pages 107–108. IEEE.

[41] Carlo Jacoboni. *Theory of electron transport in semiconductors: a pathway from elementary physics to nonequilibrium Green functions*, volume 165. Springer Science & Business Media, 2010.

[42] T. Grasser, Tang Ting-Wei, H. Kosina, and S. Selberherr. A review of hydrodynamic and energy-transport models for semiconductor device simulation. *Proceedings of the IEEE*, 91(2):251–274, 2003.

[43] Inchan Hwang, Christopher R. McNeill, and Neil C. Greenham. Drift-diffusion modeling of photocurrent transients in bulk heterojunction solar cells. *Journal of Applied Physics*, 106(9):094506, 2009.

[44] L. J. A. Koster, E. C. P. Smits, V. D. Mihailetchi, and P. W. M. Blom. Device model for the operation of polymer/fullerene bulk heterojunction solar cells. *Physical Review B*, 72(8), 2005.

[45] J. M. Foster, H. J. Snaith, T. Leijtens, and G. Richardson. A model for the operation of perovskite based hybrid solar cells: Formulation, analysis, and comparison to experiment. *SIAM Journal on Applied Mathematics*, 74(6):1935–1966, 2014.

[46] S. L. M. Van Mensfoort and R. Coehoorn. Effect of gaussian disorder on the voltage dependence of the current density in sandwich-type devices based on organic semiconductors. *Physical Review B*, 78(8), 2008.

[47] Matteo Patriarca, Patricio Farrell, Jürgen Fuhrmann, and Thomas Koprucki. Highly accurate quadrature-based scharfetter–gummel schemes for charge transport in degenerate semiconductors. *Computer Physics Communications*, 235:40–49, 2019.

[48] Dilara Abdel, Patricio Farrell, and Jürgen Fuhrmann. Assessing the quality of the excess chemical potential flux scheme for degenerate semiconductor device simulation. *Optical and Quantum Electronics*, 53(3), 2021.

[49] Thomas Koprucki, Nella Rotundo, Patricio Farrell, Duy Hai Doan, and Jürgen Fuhrmann. On thermodynamic consistency of a scharfetter–gummel scheme based on a modified thermal voltage for drift-diffusion equations with diffusion enhancement. *Optical and Quantum Electronics*, 47(6):1327–1332, 2015.

[50] Thomas Koprucki and Klaus Gärtner. Discretization scheme for drift-diffusion equations with strong diffusion enhancement. *Optical and Quantum Electronics*, 45(7):791–796, 2013.

[51] Alessandro Troisi and Giorgio Orlandi. Dynamics of the intermolecular transfer integral in crystalline organic semiconductors. *The Journal of Physical Chemistry A*, 110(11):4065–4070, 2006.

[52] S. Ciuchi, S. Fratini, and D. Mayou. Transient localization in crystalline organic semiconductors. *Physical Review B*, 83(8), 2011.

[53] I. I. Fishchuk, A. Kadashchuk, A. Bhoolokam, A. De Jamblinne De Meux, G. Pourtois, et al. Interplay between hopping and band transport in high-mobility disordered semiconductors at large carrier concentrations: The case of the amorphous oxide InGaZnO. *Physical Review B*, 93(19), 2016.

[54] Harald Oberhofer, Karsten Reuter, and Jochen Blumberger. Charge transport in molecular materials: An assessment of computational methods. *Chemical Reviews*, 117(15):10319–10357, 2017.

[55] Jenny A Nelson. *The physics of solar cells*. World Scientific Publishing Company, 2003.

[56] Raseong Kim, Xufeng Wang, and Mark Lundstrom. Notes on fermi-dirac integrals. *arXiv preprint arXiv:0811.0116*, 2008.

[57] Evan O Kane. Band structure of indium antimonide. *Journal of Physics and Chemistry of Solids*, 1(4):249–261, 1957.

[58] H Ehrenreich. Band structure and electron transport of gaas. *Physical Review*, 120(6):1951, 1960.

[59] EM Conwell and MO Vassell. High-field transport in n-type gaas. *Physical Review*, 166(3):797, 1968.

[60] Gernot Paasch and Susanne Scheinert. Charge carrier density of organics with gaussian density of states: Analytical approximation for the gauss–fermi integral. *Journal of Applied Physics*, 107(10):104501, 2010.

[61] Huanping Zhou, Qi Chen, Gang Li, Song Luo, Tze-bing Song, et al. Interface engineering of highly efficient perovskite solar cells. *Science*, 345(6196):542–546, 2014.

[62] Md Arafat Mahmud, Naveen Kumar Elumalai, Mushfika Baishakhi Upama, Dian Wang, Kah Howe Chan, et al. Low temperature processed ZnO thin film as electron transport layer for efficient perovskite solar cells. *Solar Energy Materials and Solar Cells*, 159:251–264, 2017.

[63] Jing Cao, Binghui Wu, Ruihao Chen, Youyunqi Wu, Yong Hui, et al. Efficient, hysteresis-free, and stable perovskite solar cells with ZnO as electron-transport layer: Effect of surface passivation. *Advanced Materials*, 30(11):1705596, 2018.

[64] Kwang-Ho Jung, Ja-Young Seo, Seonhee Lee, Hyunjung Shin, and Nam-Gyu Park. Solution-processed SnO2 thin film for a hysteresis-free planar perovskite solar cell with a power conversion efficiency of 19.2%. *Journal of Materials Chemistry A*, 5(47):24790–24803, 2017.

[65] Meiying Zhang, Fengmin Wu, Dan Chi, Keli Shi, and Shihua Huang. High-efficiency perovskite solar cells with poly(vinylpyrrolidone)-doped SnO2 as an electron transport layer. *Materials Advances*, 1(4):617–624, 2020.

[66] Md Bodiul Islam, Masatoshi Yanagida, Yasuhiro Shirai, Yoichi Nabetani, and Kenjiro Miyano. NiOx hole transport layer for perovskite solar cells with improved stability and reproducibility. *ACS Omega*, 2(5):2291–2299, 2017.

[67] Zijun Hu, Da Chen, Pan Yang, Lijun Yang, Laishun Qin, et al. Sol-gel-processed yttrium-doped NiO as hole transport layer in inverted perovskite solar cells for enhanced performance. *Applied Surface Science*, 441:258–264, 2018.

[68] Zafer Hawash, Luis K. Ono, and Yabing Qi. Recent advances in Spiro-MeOTAD hole transport material and its applications in organic–inorganic halide perovskite solar cells. *Advanced Materials Interfaces*, 5(1):1700623, 2018.

[69] Paramaguru Ganesan, Kunwu Fu, Peng Gao, Ines Raabe, Kurt Schenk, et al. A simple spiro-type hole transporting material for efficient perovskite solar cells. *Energy & Environmental Science*, 8(7):1986–1991, 2015.

[70] Khan Mamun Reza, Ashim Gurung, Behzad Bahrami, Sally Mabrouk, Hytham Elbohy, et al. Tailored PEDOT: PSS hole transport layer for higher performance in perovskite solar cells: Enhancement of electrical and optical properties with improved morphology. *Journal of Energy Chemistry*, 44:41–50, 2020.

[71] Yijie Xia and Shuyang Dai. Review on applications of PEDOTs and PEDOT:PSS in perovskite solar cells. *Journal of Materials Science: Materials in Electronics*, 32(10):12746–12757, 2021.

[72] Jinzhi Niu, Dong Yang, Xiaodong Ren, Zhou Yang, Yucheng Liu, et al. Graphene-oxide doped PEDOT: PSS as a superior hole transport material for high-efficiency perovskite solar cell. *Organic Electronics*, 48:165–171, 2017.

[73] Eui Hyuk Jung, Nam Joong Jeon, Eun Young Park, Chan Su Moon, Tae Joo Shin, Tae-Youl Yang, Jun Hong Noh, and Jangwon Seo. Efficient, stable and scalable perovskite solar cells using poly(3-hexylthiophene). *Nature*, 567(7749):511–515, 2019.

[74] Peng Zhou, Tongle Bu, Shengwei Shi, Lingfeng Li, Yulong Zhang, et al. Efficient and stable mixed perovskite solar cells using P3HT as a hole transporting layer. *Journal of Materials Chemistry C*, 6(21):5733–5737, 2018.

[75] Xuan Liu, Xinxin Xia, Qiuquan Cai, Feilong Cai, Liyan Yang, et al. Efficient planar heterojunction perovskite solar cells with weak hysteresis fabricated via bar coating. *Solar Energy Materials and Solar Cells*, 159:412–417, 2017.

[76] Yang Bai, Hui Yu, Zonglong Zhu, Kui Jiang, Teng Zhang, et al. High performance inverted structure perovskite solar cells based on a PCBM:polystyrene blend electron transport layer. *Journal of Materials Chemistry A*, 3(17):9098–9102, 2015.

[77] Selvakumar Pitchaiya, Muthukumarasamy Natarajan, Agilan Santhanam, Vijayshankar Asokan, Akila Yuvapragasam, et al. A review on the classification of organic/inorganic/carbonaceous hole transporting materials for perovskite solar cell application. *Arabian Journal of Chemistry*, 13(1):2526–2557, 2020.

[78] Shizhao Zheng, Gaopeng Wang, Tongfa Liu, Lingyun Lou, Shuang Xiao, et al. Materials and structures for the electron transport layer of efficient and stable perovskite solar cells. *Science China Chemistry*, 62(7):800–809, 2019.

[79] T. Jesper Jacobsson, Adam Hultqvist, Alberto García-Fernández, Aman Anand, Amran Al-Ashouri, et al. An open-access database and analysis tool for perovskite solar cells based on the fair data principles. *Nature Energy*, 7(1):107–115, 2022.

[80] Kai-Chi Hsiao, Meng-Huan Jao, Kuo-Yu Tian, Ting-Han Lin, Dinh-Phuc Tran, et al. Acetamidinium cation to confer ion immobilization and structure stabilization of organometal halide perovskite toward long life and high-efficiency p-i-n planar solar cell via air-processable method. *Solar RRL*, 4(9):2000197, 2020.

[81] R. T. Mouchou, T. C. Jen, O. T. Laseinde, and K. O. Ukoba. Numerical simulation and optimization of p-NiO/n-TiO2 solar cell system using SCAPS. *Materials Today: Proceedings*, 38:835–841, 2021.

[82] Bingjuan Zhang, Jie Su, Xing Guo, Long Zhou, Zhenhua Lin, et al. NiO/perovskite heterojunction contact engineering for highly efficient and stable perovskite solar cells. *Advanced Science*, 7(11):1903044, 2020.

[83] Mingyu Jeong, In Woo Choi, Eun Min Go, Yongjoon Cho, Minjin Kim, et al. Stable perovskite solar cells with efficiency exceeding 24.8% and 0.3V voltage loss. *Science*, 369(6511):1615–1620, 2020.

[84] Mahdi Malekshahi Byranvand, Taewan Kim, Seulki Song, Gyeongho Kang, Seung Un Ryu, et al. p-type CuI islands on TiO2 electron transport layer for a highly efficient planar-perovskite solar cell with negligible hysteresis. *Advanced Energy Materials*, 8(5):1702235, 2018.

[85] Xuemei Dong, Dong Chen, Junshuai Zhou, Yan-Zhen Zheng, and Xia Tao. High crystallization of a multiple cation perovskite absorber for low-temperature stable ZnO solar cells with high-efficiency of over 20%. *Nanoscale*, 10(15):7218–7227, 2018.

[86] Man Yue, Jie Su, Peng Zhao, Zhenhua Lin, Jincheng Zhang, et al. Optimizing the performance of CsPbI3-based perovskite solar cells via doping a ZnO electron transport layer coupled with interface engineering. *Nano-Micro Letters*, 11(1), 2019.

[87] Yizhe Sun, Weigao Wang, Heng Zhang, Qiang Su, Jiangliu Wei, et al. High-performance quantum dot light-emitting diodes based on Al-doped ZnO nanoparticles electron transport layer. *ACS Applied Materials & Interfaces*, 10(22):18902–18909, 2018.

[88] Jason J. Yoo, Gabkyung Seo, Matthew R. Chua, Tae Gwan Park, Yongli Lu, et al. Efficient perovskite solar cells via improved carrier management. *Nature*, 590(7847):587–593, 2021.

[89] Peng Zhao, Zhenhua Lin, Jiaping Wang, Man Yue, et al. Numerical simulation of planar heterojunction perovskite solar cells based on SnO2 electron transport layer. *ACS Applied Energy Materials*, 2(6):4504–4512, 2019.

[90] Di Wang, Shan-Ci Chen, and Qingdong Zheng. Poly(vinylpyrrolidone)-doped SnO2 as an electron transport layer for perovskite solar cells with improved performance. *Journal of Materials Chemistry C*, 7(39):12204–12210, 2019.

[91] Kelly A. Peterson, Ashlea Patterson, Alejandro Vega-Flick, Bolin Liao, and Michael L. Chabinyc. Doping molecular organic semiconductors by diffusion from the vapor phase. *Materials Chemistry Frontiers*, 4(12):3632–3639, 2020.

[92] Wei-Jie Chi, Quan-Song Li, and Ze-Sheng Li. Exploring the electrochemical properties of hole transport materials with spiro-cores for efficient perovskite solar cells from first-principles. *Nanoscale*, 8(11):6146–6154, 2016.

[93] James Kirkpatrick and Jenny Nelson. Theoretical study of the transfer integral and density of states in spiro-linked triphenylamine derivatives. *The Journal of Chemical Physics*, 123(8):084703, 2005.

[94] Xavier Sallenave, Mona Shasti, Elham Halvani Anaraki, Dmytro Volyniuk, Juozas Vidas Grazulevicius, et al. Interfacial and bulk properties of hole transporting materials in perovskite solar cells: spiro-MeTAD versus spiro-OMeTAD. *Journal of Materials Chemistry A*, 8(17):8527–8539, 2020.

[95] Ilhan Yavuz and K. N. Houk. Mesoscale ordering and charge-transport of crystalline Spiro-OMeTAD organic semiconductors. *The Journal of Physical Chemistry C*, 121(2):993–999, 2017.

[96] Kai Wang, Luyao Zheng, Tao Zhu, Xiang Yao, Chao Yi, et al. Efficient perovskite solar cells by hybrid perovskites incorporated with heterovalent neodymium cations. *Nano Energy*, 61:352–360, 2019.

[97] Kuan-Ying Ho, Chi-Kang Li, Hong-Jhang Syu, Yi Lai, Ching-Fuh Lin, et al. Analysis of the PEDOT:PSS/Si nanowire hybrid solar cell with a tail state model. *Journal of Applied Physics*, 120(21):215501, 2016.

[98] Jaehyung Hwang, Fabrice Amy, and Antoine Kahn. Spectroscopic study on sputtered PEDOT/PSS: Role of surface PSS layer. *Organic electronics*, 7(5):387–396, 2006.

[99] TJ Whitcher, WS Wong, AN Talik, KL Woon, N Chanlek, et al. Investigation into the gaussian density of states widths of organic semiconductors. *Journal of Physics D: Applied Physics*, 49(32):325106, 2016.

[100] Hanul Min, Maengsuk Kim, Seung-Un Lee, Hyeonwoo Kim, Gwisu Kim, et al. Efficient, stable solar cells by using inherent bandgap of α-phase formamidinium lead iodide. *Science*, 366(6466):749–753, 2019.

[101] Roderick C. I. Mackenzie, Thomas Kirchartz, George F. A. Dibb, and Jenny Nelson. Modeling nongeminate recombination in P3HT:PCBM solar cells. *The Journal of Physical Chemistry C*, 115(19):9806–9813, 2011.

[102] Yosuke Kanai and Jeffrey C. Grossman. Role of semiconducting and metallic tubes in P3HT/carbon-nanotube photovoltaic heterojunctions: Density functional theory calculations. *Nano Letters*, 8(3):908–912, 2008.

[103] Wenzhan Xu, Luyao Zheng, Xiaotao Zhang, Yu Cao, Tianyu Meng, et al. Efficient perovskite solar cells fabricated by Co partially substituted hybrid perovskite. *Advanced Energy Materials*, 8(14):1703178, 2018.

[104] Germà Garcia-Belmonte, Pablo P Boix, Juan Bisquert, Michele Sessolo, and Henk J Bolink. Simultaneous determination of carrier lifetime and electron density-of-states in P3HT: PCBM organic solar cells under illumination by impedance spectroscopy. *Solar Energy Materials and Solar Cells*, 94(2):366–375, 2010.

[105] V. D. Mihailetchi, J. K. J. Van Duren, P. W. M. Blom, J. C. Hummelen, R. A. J. Janssen, et al. Electron transport in a methanofullerene. *Advanced Functional Materials*, 13(1):43–46, 2003.

[106] Florian Steiner, Samuel Foster, Arthur Losquin, John Labram, Thomas D. Anthopoulos, et al. Distinguishing the influence of structural and energetic disorder on electron transport in fullerene multi-adducts. *Materials Horizons*, 2(1):113–119, 2015.

[107] John A. Mikroyannidis, Antonis N. Kabanakis, S. S. Sharma, and Ganesh D. Sharma. A simple and effective modification of PCBM for use as an electron acceptor in efficient bulk heterojunction solar cells. *Advanced Functional Materials*, 21(4):746–755, 2011.

[108] Gilles Horowitz. Validity of the concept of band edge in organic semiconductors. *Journal of Applied Physics*, 118(11):115502, 2015.

[109] Alejandra Castro-Chong, Antonio J. Riquelme, Tom Aernouts, Laurence J. Bennett, Giles Richardson, et al. Illumination intensity dependence of the recombination mechanism in mixed perovskite solar cells. *ChemPlusChem*, 86(9):1347–1356, 2021.

[110] Will Clarke, Laurence J. Bennett, Yoana Grudeva, Jamie M. Foster, Giles Richardson, and Nicola E. Courtier. Ionmonger 2.0: software for free, fast and versatile simulation of current, voltage and impedance response of planar perovskite solar cells. *Journal of Computational Electronics*, 2022.

[111] Adam Pockett, Giles E Eperon, Nobuya Sakai, Henry J Snaith, Laurence M Peter, and Petra J Cameron. Microseconds, milliseconds and seconds: deconvoluting the dynamic behaviour of planar perovskite solar cells. *Physical Chemistry Chemical Physics*, 19(8):5959–5970, 2017.

[112] Laurence J. Bennett, Antonio J. Riquelme, Juan A. Anta, Nicola E. Courtier, and Giles Richardson. Avoiding ionic interference in computing the ideality factor for perovskite solar cells and an analytical theory of their impedance-spectroscopy response. *Physical Review Applied*, 19(1), 2023.

[113] Mark E Orazem and Bernard Tribollet. Electrochemical impedance spectroscopy. *New Jersey*, pages 383–389, 2008.

[114] Federico Brivio, Keith T. Butler, Aron Walsh, and Mark Van Schilfgaarde. Relativistic quasiparticle self-consistent electronic structure of hybrid halide perovskite photovoltaic absorbers. *Physical Review B*, 89(15), 2014.

[115] Philipp Löper, Michael Stuckelberger, Bjoern Niesen, Jérémie Werner, Miha Filipič, et al. Complex refractive index spectra of CH3NH3PbI3 perovskite thin films determined by spectroscopic ellipsometry and spectrophotometry. *The Journal of Physical Chemistry Letters*, 6(1):66–71, 2015.

[116] Philip Schulz, Eran Edri, Saar Kirmayer, Gary Hodes, David Cahen, et al. Interface energetics in organo-metal halide perovskite-based photovoltaic cells. *Energy & Environmental Science*, 7(4):1377, 2014.

[117] Constantinos C. Stoumpos, Christos D. Malliakas, and Mercouri G. Kanatzidis. Semiconducting tin and lead iodide perovskites with organic cations: Phase transitions, high mobilities, and near-infrared photoluminescent properties. *Inorganic Chemistry*, 52(15):9019–9038, 2013.

[118] Moritz H. Futscher, Ju Min Lee, Lucie McGovern, Loreta A. Muscarella, Tianyi Wang, et al. Quantification of ion migration in CH3NH3PbI3 perovskite solar cells by transient capacitance measurements. *Materials Horizons*, 6(7):1497–1503, 2019.

[119] Zhe Xu, Jihuai Wu, Tongyue Wu, Quanlin Bao, Xin He, Zhang Lan, Jianming Lin, Miaoliang Huang, Yunfang Huang, and Leqin Fan. Tuning the fermi level of tio¡sub¿2¡/sub¿ electron transport layer through europium doping for highly efficient perovskite solar cells. *Energy Technology*, 5(10):1820–1826, 2017.

[120] H Wang, Guoguang Wu, XP Cai, Y Zhao, ZF Shi, et al. Effect of growth temperature on structure and optical characters of NiO films fabricated by PA-MOCVD. *Vacuum*, 86(12):2044–2047, 2012.

[121] Guozhan Xia, Boyuan Huang, Ying Zhang, Xingyu Zhao, Chen Wang, Chunmei Jia, Jinjin Zhao, Weiqiu Chen, and Jiangyu Li. Nanoscale insights into photovoltaic hysteresis in triple-cation mixed-halide perovskite: Resolving the role of polarization and ionic migration. *Advanced Materials*, 31(36):1902870, 2019.

Appendix A: The full charge transport model

Here we list the full charge transport model of a three-layer perovskite solar cell. Equations directly modified to account for full Fermi-Dirac statistics are highlighted in teal. This charge transport model was presented in [110].

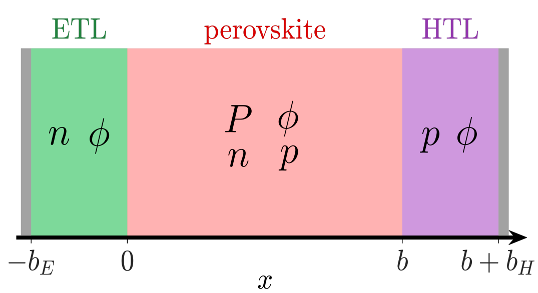

FIG. 9. Schematic of the three-layer planar drift-diffusion model of a PSC.

a. Perovskite absorber layer ($0 < x < b$)

$$\frac{\partial P}{\partial t} + \frac{\partial F^P}{\partial x} = 0 \qquad F^P = -D_I\left(\frac{\partial P}{\partial x} + \frac{P}{V_T}\frac{\partial \phi}{\partial x}\right) \tag{A1}$$

$$\frac{\partial n}{\partial t} - \frac{1}{q}\frac{\partial j^n}{\partial x} = G(x,t) - R(n,p) \qquad j^n = qD_n\left(\frac{\partial n}{\partial x} - \frac{n}{V_T}\frac{\partial \phi}{\partial x}\right) \tag{A2}$$

$$\frac{\partial p}{\partial t} + \frac{1}{q}\frac{\partial j^p}{\partial x} = G(x,t) - R(n,p) \qquad j^p = -qD_p\left(\frac{\partial p}{\partial x} + \frac{p}{V_T}\frac{\partial \phi}{\partial x}\right) \tag{A3}$$

$$\frac{\partial^2 \phi}{\partial x^2} = \frac{q}{\varepsilon_A}(N_0 - P + n - p) \tag{A4}$$

where G and R are the generation and recombination rates.

b. Electron transport layer ($-b_E < x < 0$)

$$\frac{\partial n}{\partial t} - \frac{1}{q}\frac{\partial j^n}{\partial x} = 0 \qquad j^n = \mu_E k_B T n \frac{\partial}{\partial x}\left[\mathcal{S}_E^{-1}\left(\frac{n}{g_c^E}\right) - \frac{\phi}{k_B T}\right] \tag{A5}$$

$$\frac{\partial^2 \phi}{\partial x^2} = \frac{q}{\varepsilon_E}(n - d_E) \tag{A6}$$

c. Hole transport layer ($b < x < b + b_H$)

$$\frac{\partial p}{\partial t} + \frac{1}{q}\frac{\partial j^p}{\partial x} = 0 \qquad j^p = -\mu_H k_B T p \frac{\partial}{\partial x}\left[\mathcal{S}_H^{-1}\left(\frac{p}{g_v^H}\right) + \frac{\phi}{k_B T}\right] \tag{A7}$$

$$\frac{\partial^2 \phi}{\partial x^2} = \frac{q}{\varepsilon_E}(d_H - p) \tag{A8}$$

d. Boundary conditions

$$n|_{x=-b_E} = d_E, \qquad \phi|_{x=-b_E} = \frac{V_{bi} - V(t)}{2} \tag{A9}$$

$$p|_{x=b+b_H} = d_H, \qquad \phi|_{x=b+b_H} = -\frac{V_{bi} - V(t)}{2} \tag{A10}$$

e. Continuity conditions

$$\left.\begin{aligned} j^n|_{x=0^-} &= j^n|_{x=0^+} - R_l \\ j^p &= -qR_l \\ F^P &= 0 \\ \phi|_{x=0^-} &= \phi|_{x=0^+} \\ \varepsilon_E \frac{\partial \phi}{\partial x}\Big|_{x=0^-} &= \varepsilon_A \frac{\partial \phi}{\partial x}\Big|_{x=0^+} \\ d_E k_E \exp\left[\mathcal{S}_E^{-1}\left(\frac{n|_{x=0^-}}{g_c^E}\right) - \mathcal{S}_E^{-1}\left(\frac{d_E}{g_c^E}\right)\right] &= n|_{x=0^+} \end{aligned}\right\} \text{ on } \ x = 0 \tag{A11}$$

$$\left.\begin{aligned} j^p|_{x=b^-} - R_r &= j^p|_{x=b^+} \\ j^n &= -qR_r \\ F^P &= 0 \\ \phi|_{x=b^-} &= \phi|_{x=b^+} \\ \varepsilon_A \frac{\partial \phi}{\partial x}\Big|_{x=b^-} &= \varepsilon_H \frac{\partial \phi}{\partial x}\Big|_{x=b^+} \\ p|_{x=b^-} &= d_H k_H \exp\left[\mathcal{S}_H^{-1}\left(\frac{p|_{x=b^+}}{g_v^H}\right) - \mathcal{S}_H^{-1}\left(\frac{d_H}{g_v^H}\right)\right] \end{aligned}\right\} \text{ on } \ x = b \tag{A12}$$

where

$$k_E = \frac{g_c}{d_E}\exp\left(\frac{E_c^E - E_c}{k_B T} + \mathcal{S}_E^{-1}\left(\frac{d_E}{g_c^E}\right)\right) \tag{A13}$$

$$k_H = \frac{g_v}{d_H}\exp\left(\frac{E_v - E_v^H}{k_B T} + \mathcal{S}_H^{-1}\left(\frac{d_H}{g_v^H}\right)\right) \tag{A14}$$

Appendix B: Parameter set

Symbol	Name	Values	Unit	Ref.
T	Temperature	298	K	
-	Light entering through	ETL	-	
Perovskite (MAPI)				
b	Perovskite width	400	nm	
ε_p	Permittivity	24.1	ε_0	[114]
α	Absorption coefficient	1.3×10^7	m^{-1}	[115]
g_c	Conduction band effective DoS	$8.1{\times}10^{24}$	m^{-3}	[114]
g_v	Valence band effective DoS	5.8×10^{24}	m^{-3}	[114]
E_c	Conduction band edge	-3.7	eV	[116]
E_v	Valence band edge	-5.4	eV	[116]
D_n	Electron diffusivity	$1.7{\times}10^{-4}$	m^2s^{-1}	[117]
D_p	Hole diffusivity	$1.7{\times}10^{-4}$	m^2s^{-1}	[117]
N_0	Mean anion vacancy density	1.6×10^{25}	m^{-3}	[118]
D_P	Anion vacancy diffusivity	$1{\times}10^{-17}$	m^2s^{-1}	[9]
ETL (TiO_2)				
g_c^E	Conduction band effective DoS	2×10^{23}	m^{-3}	[81]
E_f^E	Equilibrium electron QFL	-4.19	eV	[119]
D_E	Electron diffusivity	1.3×10^{-5}	m^2s^{-1}	[120]
ε_E	Permittivity	10	ε_0	
b_E	ETL width	100	nm	[121]
E_c^E	Conduction band edge	-4.13	eV	[84]
HTL (spiro-MeOTAD)				
g_v^H	Valence band effective DoS	1×10^{26}	m^{-3}	[91]
E_f^H	Equilibrium hole QFL	-4.97	eV	
D_H	Hole diffusivity	1×10^{-6}	m^2s^{-1}	[120]
ε_H	Permittivity	3	ε_0	
b_H	HTL width	200	nm	[121]
E_v^H	Valence band edge	-5.1	eV	[92]

TABLE II. Material parameters for a TiO_2/MAPI/spiro-MeOTAD cell. The necessary parameters to model non-Boltzmann statistics in the transport layers are shown in Table I.

Symbol	Name	Values	Unit
Perovskite bulk			
β	Bi-molecular rate constant	$1.5{\times}10^{-14}$	m^3s^{-1}
τ_p	Hole SRH psuedo-lifetime	$3{\times}10^{-7}$	s
τ_n	Electron SRH psuedo-lifetime	$3{\times}10^{-7}$	s
A_n	Electron Auger coefficient	0	m^6s^{-1}
A_p	Hole Auger coefficient	0	m^6s^{-1}
ETL/perovskite interface			
ν_p^E	Hole recombination velocity	10	ms^{-1}
ν_n^E	Electron recombination velocity 0	10^5	ms^{-1}
β_E	Bi-molecular rate constant	0	m^4s^{-1}
HTL/perovskite interface			
ν_p^H	Hole recombination velocity	10^5	ms^{-1}
ν_n^H	Electron recombination velocity	0.1	ms^{-1}
β_H	Bi-molecular rate constant	0	m^4s^{-1}

TABLE III. Recombination parameters for a typical TiO_2/MAPI/spiro-MeOTAD cell.